

Article

On a Flood-Producing Coastal Mesoscale Convective Storm Associated with the Kor'easterlies: Multi-Data Analyses Using Remotely-Sensed and In-Situ Observations and Storm-Scale Model Simulations

Seon Ki Park ^{1,2,3,4,*}  and Sojung Park ^{2,3,4}¹ Department of Environmental Science and Engineering, Ewha Womans University, Seoul 03760, Korea² Department of Climate and Energy Systems Engineering, Ewha Womans University, Seoul 03760, Korea; sjpark1228@ewhain.net³ Severe Storm Research Center, Ewha Womans University, Seoul 03760, Korea⁴ Center for Climate/Environment Change Prediction Research and Severe Storm Research Center, Ewha Womans University, Seoul 03760, Korea

* Correspondence: spark@ewha.ac.kr; Tel.: +82-2-3277-3331

Received: 23 March 2020; Accepted: 6 May 2020 ; Published: 11 May 2020



Abstract: A flood-producing heavy rainfall event occurred at the mountainous coastal region in the northeast of South Korea on 5–6 August 2018, subsequent to extreme heat waves, through a quasi-stationary mesoscale convective system (MCS). We analyzed the storm environment via a multi-data approach using high-resolution (1-km) simulations from the Weather Research and Forecasting (WRF) and in situ/satellite/radar observations. The brightness temperature, from the Advanced Himawari Imager water vapor band, and the composite radar reflectivity were used to identify characteristics of the MCS and associated precipitations. The following factors affected this back-building MCS: low-level convergence by the Korea easterlies (Kor'easterlies), carrying moist air into the coast; strong vertical wind shear, making the updraft tilted and sustained; coastal fronts and back-building convection bands, formed through interactions among the Kor'easterlies, cold pool outflows, and orography; mid-level advection of cold air and positive relative vorticity, enhancing vertical convection and potential instability; and vigorous updraft releasing potential instability. The pre-storm synoptic environment provided favorable conditions for storm development such as high moisture and temperature over the coastal area and adjacent sea, and enhancement of the Kor'easterlies by expansion of a surface high pressure system. Upper-level north-northwesterly winds prompted the MCS to propagate south-southeastward along the coastline.

Keywords: mesoscale convective system; the Korea easterlies; back-building convection; tapering cloud; heavy rainfall

1. Introduction

The eastern coastal region of South Korea has complex terrain with a narrow coastal area surrounded by the East Sea/Sea of Japan (hereafter, ES) and a steep and long mountain range parallel to the coastline. This region, named *Yeongdong*, often experiences hazardous weather phenomena—generally associated with transport of moist air from the ES by the so-called “Korea easterlies” (hereafter, the Kor'easterlies), and their associated orographic lifting (e.g., [1–4]). The Kor'easterlies, locally named *Donghae-poong* (meaning winds from the ES in Korean), are defined as low-level moist airflows from the ES, mostly below 700 hPa, causing weather hazards such as heavy rainfall/snowfall, fog, and low temperature at the mountainous coastal areas in Yeongdong [5].

In mountainous coastal regions, heavy precipitation events occur often in association with factors such as instability enhancement, cold air damming, barrier jets parallel to the mountain range, low-level convergence and moisture transport by prevailing winds, orographic lifting, etc. (e.g., [1,3,6–9]).

Flash floods are often induced by back-building/quasi-stationary events that produce prolonged heavy precipitation [10]. In the “back-building” process, convective cells form subsequently on the upwind side in accordance with storm motion, thus shown to be stationary or move backward [11]. Sometimes they present a tapering cloud system, encompassing deep cumulonimbi (usually brightness temperature $T_B < -40$ °C) that form at an upwind base tip and spread horizontally to the downwind side one after another (i.e., back-building): heavy rainfall concentrates on a specific area when this system stagnates or travels slowly [12].

Such flood-producing back-building convective systems frequently develop over mountainous coastal regions (e.g., [13–17]), where topography and surface characteristics play important roles in convection initiation. Orographic lifting of the conditionally unstable low-level flow impinging from marine to coastal regions and mountain foothills is able to trigger convective cells repeatedly at the same location (e.g., [18,19]). Low-level cold pools formed under mesoscale convective systems (MCSs) can also elevate the surrounding low-level flow at the leading edge of the cold front [13]. Besides these mechanical lifting processes, differential heating over heterogeneous surfaces induces thermodynamically-driven lifting and influences development and propagation of storms (e.g., [20,21]).

Prevailing winds (e.g., the Kor’easterlies) also influence low-level convergence, moisture/heat transport, and orographic lifting: the wind characteristics strongly depend upon the synoptic patterns and circulation systems at the local region. Therefore, in order to improve the forecast skill of hazardous weather systems in mountainous coastal regions around the world as well as Yeongdong, Korea, it is essential to study not only the characteristics of the convective systems but also the occurrence and coastal/inland incursion of prevailing winds.

Recently, Japan has suffered from the so-called “Heavy Rain Event of July 2018” (officially named by the Japan Meteorological Agency), followed by an extreme heat wave (e.g., [22,23]). The extreme rainfall was caused by persistent moist airflows and Baiu frontal ascent [22,24], and extreme moisture content at the middle levels [25]. Reference [24] pointed out global warming as a possible cause of heavy rainfall through the super Clausius–Clapeyron relationship (e.g., [26]).

In these days, abundant data are available for studying various aspects of atmospheric phenomena. Multi-sensor and/or multi-platform remote sensing approach has been very useful in monitoring and assessing diverse systems in weather/climate, agriculture, environment, etc. (e.g., [27–31]). Multi-data approach, using both observations and numerical model, has been applied to examine assorted aspects of severe convective events (e.g., [29,32–35]) as well as environmental monitoring and prediction (e.g., [36,37]).

In this study, through the multi-data approach using in-situ and satellite/radar data and high-resolution model simulations, we investigate a Kor’easterlies-induced heavy rainfall event of 5–6 August 2018 that caused a flash flood in Yeongdong, Korea, subsequent to a prolonged extreme heat wave. It accompanied a tapering cloud system, rarely observed in Korea, and was associated with a quasi-stationary MCS. Because this kind of consecutive extreme events of contrasting nature was unprecedented in Korea but would possibly occur more frequently in the future, not only in Korea but also in many places around the world, it is essential to understand the mechanism of the flood-producing coastal convective system under extremely warm atmospheric environment. Section 2 describes the details of the numerical simulation and observation data. Section 3 describes the study case and the model validation while Section 4 discusses the major findings on the storm environment and the processes related to its initiation, back-building development and termination. Section 5 provides conclusions.

2. Method and Data

2.1. Numerical Simulation

We employed the Advanced Research Weather Research and Forecasting (WRF-ARW) model version 4.0 over a two-way interacting triply-nested domain—d01 (outermost) to d03 (innermost)—with d01 centered at 37.5°N and 130°E in the Lambert conformal conic projection. The model was initialized at 00:00 UTC (09:00 KST; Korea Standard Time) 5 August 2018 with the initial and boundary conditions provided by the 6-hourly National Center for Environmental Prediction (NCEP) Final (FNL) Operational Model Global Tropospheric Analyses data on 1° × 1° grids. Computational domain and model configurations are depicted in Figure 1 and Table 1, respectively. We adopted the Morrison double-moment microphysics scheme [38], which has double moments in four hydrometeors—rain, ice, snow, and graupel—because it is generally believed that double-moment schemes outperform single-moment schemes [39].

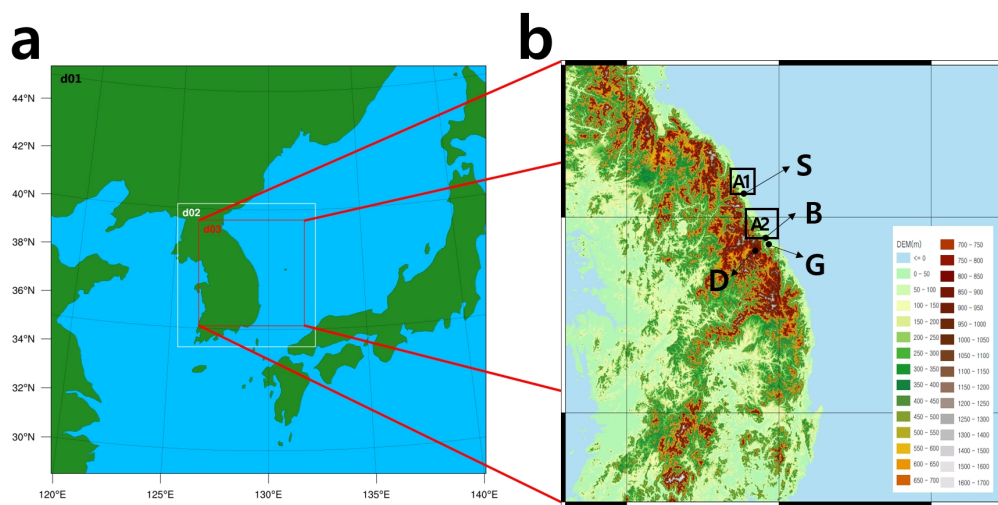


Figure 1. (a) Computational domains with triple nesting (d01, d02, and d03) and (b) topography of d03 (shaded) with the height range represented in m above sea level (asl). In (b), black boxes are for area-averaged analyses, representing areas of upwind tips of tapering clouds near Sokcho (A1) and Bukgangneung (A2), whereas black dots depict locations of weather stations: Sokcho (S; 38.25°N, 128.56°E; 18.06 m asl), Bukgangneung (B; 37.80°N, 128.86°E; 78.9 m asl), Gangneung (G; 37.75°N, 128.89°E; 26.04 m asl), and Daegwallyeong (D; 37.68°N, 128.86°E; 772.57 m asl). Topography data are from the Advanced Spaceborne Thermal Emission and Reflection Radiometer (ASTER) Global Digital Elevation Model (GDEM), available at <https://earthdata.nasa.gov/>.

Table 1. Summary of the Weather Research and Forecasting (WRF) model configuration.

	Domain d01	Domain d02	Domain d03
Horizontal grid spacing	25 km	5 km	1 km
Horizontal grid points	80 × 75	126 × 131	481 × 481
Vertical levels/Model top		80 levels/50 hPa	
Vertical coordinate		Hybrid sigma-pressure (default)	
Time step	150 s	30 s	6 s
Forecast time		32 h starting at 00:00 UTC 5 August 2018	
Microphysics		Morrison double moment [38]	
Radiation		Longwave: RRTM [40]; Shortwave: Dudhia [41]	
Surface physics		Community Land Model version 4 (CLM4) [42,43]	
Planetary Boundary Layer		Yonsei University (YSU) [44]	
Cumulus		Kain-Fritsch (new Eta) [45]	None
Initial/Boundary condition		NCEP FNL Operational Model Global Tropospheric Analyses	

2.2. Observation Data

We have used various observation data collected from the Korea Meteorological Administration (KMA). The KMA operates a dense surface observation network with an average space resolution of about 13 km—a total of 590 stations with 96 Automated Synoptic Observing Systems (ASOSs) and 494 Automatic Weather Systems (AWSs). The ASOS is installed at a manned observing station while the AWS is an unmanned observing tower installed in high mountains or on isolated islands. The AWS measures temperature, pressure, humidity, wind and precipitation while the ASOS measures a total of 16 elements such as cloud coverage and base height, solar radiation, visibility, etc., including those from the AWS—both observations are made every minute. The KMA also has a lightning detection network of 21 sites that measures the time, location, strength, elevation, etc., of lightning strokes, with a median accuracy within 250 m and detection efficiency higher than 95% over the Korean Peninsula and its adjacent seas. We used the data set from the ASOS and AWS networks, the lightning detection network, and the vertical rawinsonde sounding at Bukgangneung for observational analyses and model validation.

We have also employed the composite radar reflectivity data, attained from 11 KMA radars, on the plan position indicator (PPI) display after quality control, with horizontal and temporal resolutions of 1 km and 10 min, respectively. In addition, for the validation purpose, we used the composite precipitation data produced by the KMA Radar-AWS Rain-rate (RAR) calculation system [46]. The RAR data cover 1241 km × 1761 km over the Korean Peninsula, with a grid size of 1 km and a time resolution of 10 min, and have been employed for many precipitation analysis studies in Korea (e.g., [47–49]). Note that rain-rate estimates by radar only have considerable systematic and random errors; thus having limited hydrological applications than rain gauge data [50]. The RAR-estimated rainfall obtained a squared correlation coefficient $R^2 = 0.84$ with the observed daily accumulated rainfall [46]; further improvement was made in the correlation coefficient up to 11.7% through bias corrections [48].

Besides, to identify deep convective clouds, we analyzed T_B obtained from the Himawari-8 water vapor bands. The Advanced Himawari Imager (AHI) [51] onboard Himawari 8 has 16 bands, including three water vapor absorption bands 8, 9, and 10 with corresponding wavelengths of 6.2, 6.9, and 7.3 μm , respectively, which produce T_B . The East Asia region is covered by the full-disk images with higher spatial and temporal resolution, taken every 10 min with a spatial resolution of 2 km. In this study, we analyzed T_B from the AHI band 8. The AHI water vapor bands are calibrated with an accuracy within 0.2 °K [51,52], and have been utilized in many studies on convective systems over East Asia (e.g., [53–55]).

2.3. Parameters for Thunderstorm Potential and Lifting Forcing

We calculated three parameters related to instability and storm possibility: Convective Available Potential Energy (CAPE), K-index (KI) [56], and Severe Weather Threat Index (SWEAT) [57]. The CAPE is related to the parcel buoyancy: for the CAPE value around 2000 J kg⁻¹, strong and severe thunderstorms are likely to develop over the Great Plains in the United States. In Korea, however, strong thunderstorms may develop with the CAPE value of 900–1800 J kg⁻¹ and severe thunderstorms with that over 1800 J kg⁻¹. Reference [58] examined 82 heavy rainfall cases in Korea and found that the CAPE values distributed below 2500 J kg⁻¹ with the average value of 850 J kg⁻¹.

The KI measures thunderstorm potential based on the lapse rate and the vertical extent of low-level moisture. The KI value over 20 means some potential for thunderstorms, that over 30 moderate potential for thunderstorms with heavy rain, and that over 40 high potential for thunderstorms with very heavy rain. The SWEAT combines kinematic and thermodynamic information (e.g., low- and mid-level wind speeds, veering, low-level moisture, instability, etc.), and is used to assess severe storm potential. The SWEAT value over 250 indicates a potential for strong convection, and that over 300 implies great possibility of severe thunderstorms.

As this heavy rainfall event (HRE) occurred under extremely warm environment, we suppose that the heat-induced buoyancy exerted appreciable impact on convection. To identify the relative

importance between mechanical and thermodynamically-driven lifting forcing, we calculated the gradient Richardson number (R_i), defined as the ratio of static stability (N^2) to dynamic stability (S^2), where N is the buoyancy and S is the vertical shear of horizontal wind [59].

3. Case Description and Model Validation

A flash flood occurred in Yeongdong, Korea, due to a quasi-stationary MCS that produced heavy rainfall on the evening of 5 through the nighttime of 6 August 2018. Total rainfalls of the four stations in Yeongdong, from the start to the end of precipitation, amounted to 294.7 mm at Sokcho (11:00 UTC 5–14:00 UTC 6), 205.2 mm at Bukgangneung (15:00 UTC 5–19:00 UTC 6), 200.0 mm at Gangneung (17:00 UTC 5–13:00 UTC 6), and 54.6 mm at Daegwallyeong (18:00 UTC 5–19:00 UTC 6), respectively. Maximum precipitation rates at Sokcho and Gangneung were 54.9 and 79.0 mm/h, respectively. Daily precipitation of 226.2 mm was recorded at Sokcho on 6 August 2018—second only to the one on 31 August 2002 (295.5 mm) associated with the typhoon-induced Kor’easterlies and orographic effect [1].

The simulation results agreed generally well with the observations, in terms of the accumulated rainfalls (ARs) over Yeongdong (Figure 2). Both the 12 h and 27 h ARs (Figure 2a,b) depicted the observed features well at three stations (S, G and D). In the quantitative aspect, the 12 h ARs at S from AWS, RAR and WRF were 260.9 mm, 214.5 mm and 115.1 mm, respectively: those at G were 49.0 mm, 31.6 mm and 61.2 mm, respectively: those at D were 0.0 mm, 20.9 mm and 7.0 mm, respectively. The model overestimated the 27 h AR over the coastal areas at the south of Yeongdong (Figure 2b). Overall, WRF simulated the general features of this HRE reasonably well; thus, we used the model results from d03 (1-km resolution) for storm-scale analyses.

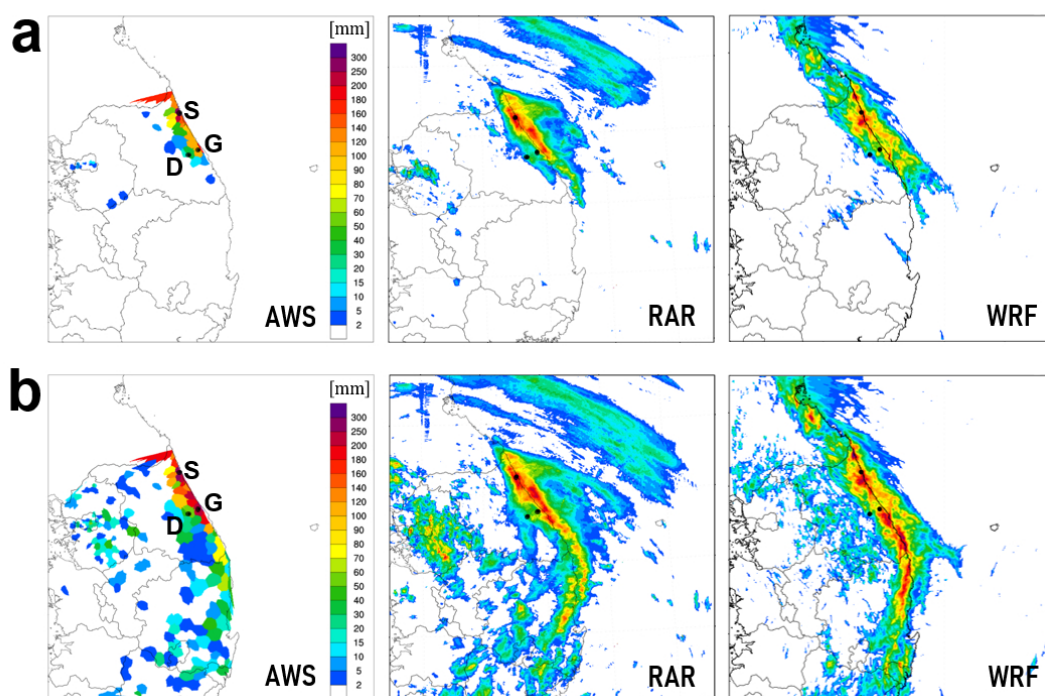


Figure 2. Accumulated rainfall amount (in mm) from the Automatic Weather Systems (AWS) observations, including the Automated Synoptic Observing Systems (ASOS), the composite radar-AWS rain-rate (RAR) data, and the model results (WRF) for (a) 12 h from 12:00 UTC 5 to 00:00 UTC 6 and (b) 27 h from 12:00 UTC 5 to 15:00 UTC 6 August 2018. Black dots depict station locations (see Figure 1b). Computations were made at the domain d03 of WRF.

4. Results

4.1. Synoptic Environment

This HRE occurred in a synoptic environment that induced the Kor'easterlies. On 12:00 UTC 5 August 2018, at the surface (Figure 3; top panel), high pressure systems were located over Northeast China (H_{NC}) and the East China Sea (H_{ECS}), whereas a low pressure system dwelt off the coast of Tohoku/Chubu, Japan (L_{TC}). During the last 24 h, H_{NC} continuously strengthened and extended southward (see the 1008 hPa isobars) while L_{TC} remained almost stationary; thus the pressure gradient over the ES increased with time, making the Kor'easterlies enhance. Westerlies prevailed over the inland due to H_{ECS} .

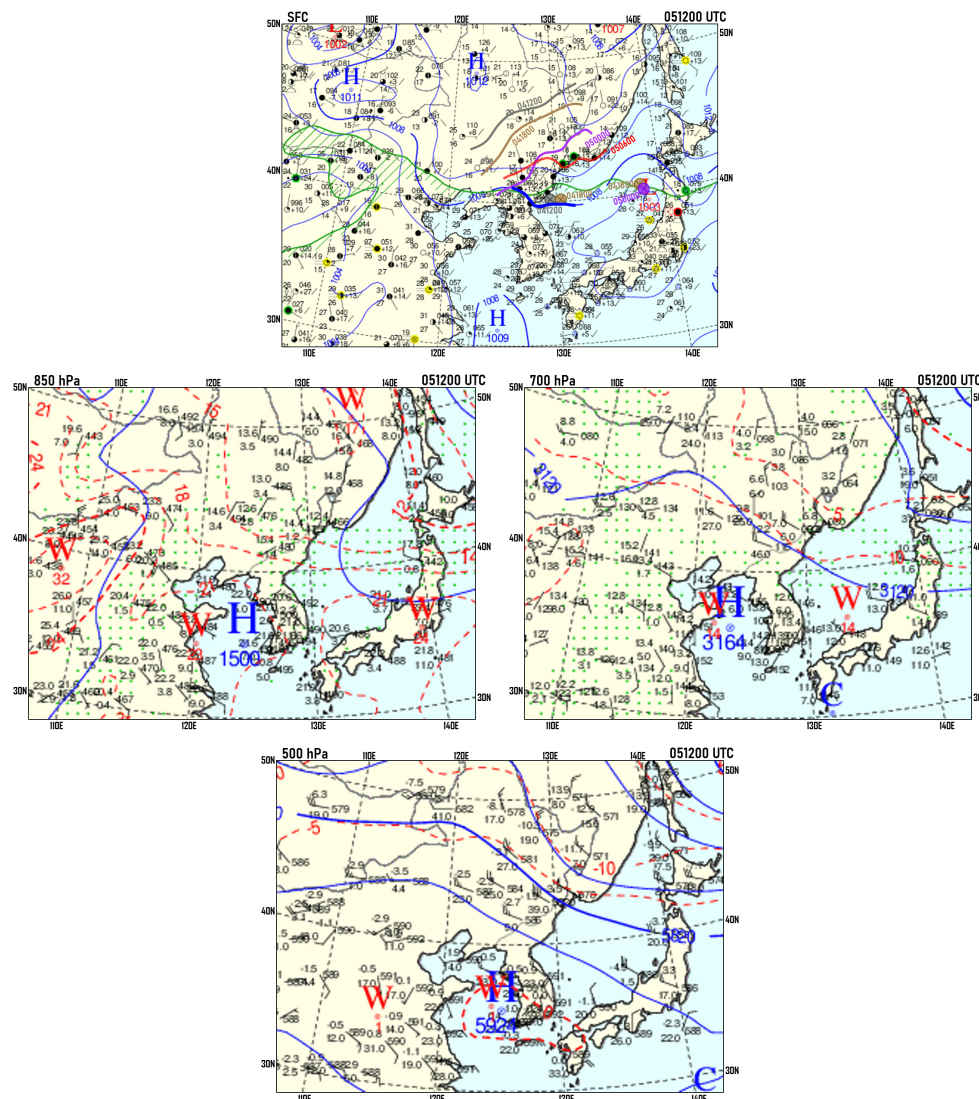


Figure 3. Surface chart (top) and upper-level charts of 850 hPa (middle left), 700 hPa (middle right), and 500 hPa (bottom) on 12:00 UTC 5 August 2018. At the surface, thick colored lines represent the 1008 hPa isobars—blue at the current time and other colors at given previous times (e.g., 050000 in violet means 00:00 UTC 5 August 2018). The colored \otimes symbols represent the center locations of low pressure systems at given previous times. Green hatched lines represent isodrosotherms of 20 °C. Stations with fog, precipitation and thunderstorm are represented by yellow, green and red circles, respectively. At the upper levels, blue solid lines represent isohypses and red dashed lines isotherms. Areas with green dots indicate wet areas with $T - T_d < 4$ °C. Modified from the Korea Meteorological Administration (KMA) weather charts.

At upper levels (Figure 3; middle and bottom panels), the Korean Peninsula was generally under the influence of a ridge with a warm-core high lingered over the Yellow Sea. A weak trough of 500 hPa over Primorsky Krai, Russia, moved to Tohoku by 00:00 UTC 6, whereas that of 700 hPa dwelt over the western coast of Chubu, Japan. In this period, a low at 850 hPa anchored over Tohoku, and extended to the central ES and Kanto/Chubu, Japan, promoting northeasterlies (i.e., the Kor'easterlies) over the northern ES and northwesterlies over the southern ES. Over the ES, at both 700 hPa and 500 hPa, isotherms were nearly parallel to isohypses with weak gradient, under prevailing northwesterlies. On the contrary, at 850 hPa, isotherms crossed isohypses over the ES with relatively strong gradient, leading to cold advection by the Kor'easterlies: the 18 °C isotherm moved southward from the northern to central part of the Korean Peninsula on the ES side. Furthermore, at both 850 and 700 hPa, the Korean side of the ES was occupied by wet areas (green dots; $T - T_d < 4$ °C).

Furthermore, heat waves lingered for several days in Yeondong just before the HRE, with record-breaking maximum temperatures at Sokcho (38.7 °C) and Bukgangneung (37.1 °C) on 5 August. The minimum temperature on the same day was 25.1 °C at Gangneung where tropical nights persisted on 2–5 August. Combined with high moisture, this situation brings high equivalent (or wet-bulb) potential temperature near surface. Along with the cold advection aloft, this environment enhances both static instability and potential (convective) instability in the planetary boundary layer (PBL).

Figure 4 shows vertical soundings of Bukgangneung. On 00:00 UTC 5 August, a weak capping inversion existed at 840–780 hPa with the convective inhibition (CIN) of 382 J kg^{-1} and CAPE of 278 J kg^{-1} , thus convection was strongly inhibited: vigorous convective outbreak occurs when the capping inversion is broken [60]. On 12:00 UTC 5, both the lifting condensation level (LCL) and the level of free convection (LFC) lowered and the atmospheric layer below 700 hPa got much wetter than 12 h earlier. The CIN decreased to 50 J kg^{-1} , revealing weak inhibition of convection, while CAPE increased to 1088 J kg^{-1} . Under these conditions, convective clouds develop instantly with proper triggering mechanisms. This sounding also depicted two LFCs, and consequently two equilibrium levels (ELs), implying that the convection can reach only up to EL1 when the updraft is not so strong while a deep convection can form when the upward forcing is strong enough to lift the saturated air parcel passing LFC2. On 00:00 UTC 6, LCL was as low as 975 hPa, and the whole atmosphere was completely saturated ($T = T_d$) except near the surface, indicating the development of a deep convective cloud.

Overall, we notice no conceivable development of a synoptic scale cyclone to produce heavy rainfall at Yeongdong; nevertheless, the synoptic environment revealed some favorable conditions for convective storm development, including: (1) high moisture and temperature over the coastal areas and adjacent sea; (2) enhancement of the Kor'easterlies transporting moisture to inland; (3) potential increase of static/convective instability at the PBL; and (4) veering vertical wind shear. Sounding analyses depicted high CIN and capping inversion during the pre-storm period, and high CAPE and lower LCL/LFC during the storm outbreak; thus the energy and instability could have been stored in the PBL, then released as severe convection via lifting forcings sufficiently strong to overcome CIN (e.g., [60]). In our case, several factors existed for the lifting forcing (i.e., triggering), including: (1) the low-level (speed) convergence; (2) orographic lifting by the coastal terrain; (3) mesoscale convergence by local circulation systems, e.g., sea/land breezes and/or mountain/valley breezes; and (4) thermodynamically-driven convection by heated land surface due to prolonged heat waves. As this HRE was related to a quasi-stationary MCS, outflows from the precipitation-induced cold pool can also trigger new convective cells. Reference [61] reported that an increase by 1 standard deviation (σ) of CAPE, relative humidity and vertical wind shear, respectively, can extend lifetime of MCSs by 3 h to 27–30 h.

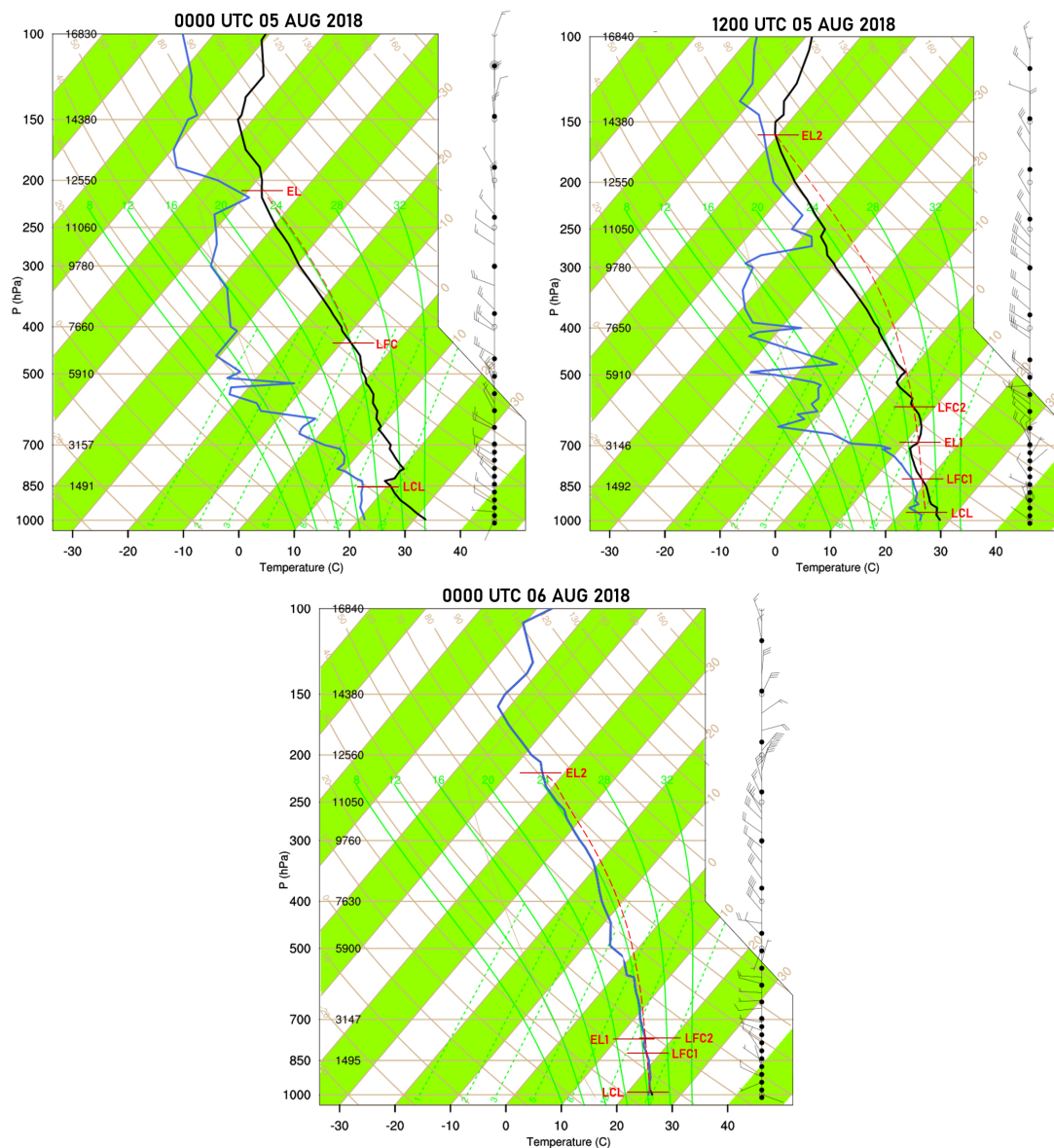


Figure 4. Skew T-log P diagrams of Bukgangneung on 00:00 UTC 5, 12:00 UTC 5, and 00:00 UTC 6 August 2018.

4.2. Mesoscale Features of the Heavy Rainfall System

4.2.1. Characteristics of Meteorological Elements and Rainfalls

Temporal variations of meteorological observations at three ASOS stations (S, G and D) are examined (Figure 5). All stations showed abrupt changes in temperature and relative humidity, accompanied by changes in winds, about 6–10 h before rainfalls occurred (see the dashed boxes in Figure 5). After these prompt changes, relative humidity steadily increased and stayed at about 97% throughout the HRE. For S and G at the coast, the sudden changes in temperature and humidity are mainly due to intrusion of the ocean air by enhancement of the Kor'easterlies. For the mountain site D, those changes occurred in two steps as a combined effect of radiation cooling and advection by the Kor'easterlies.

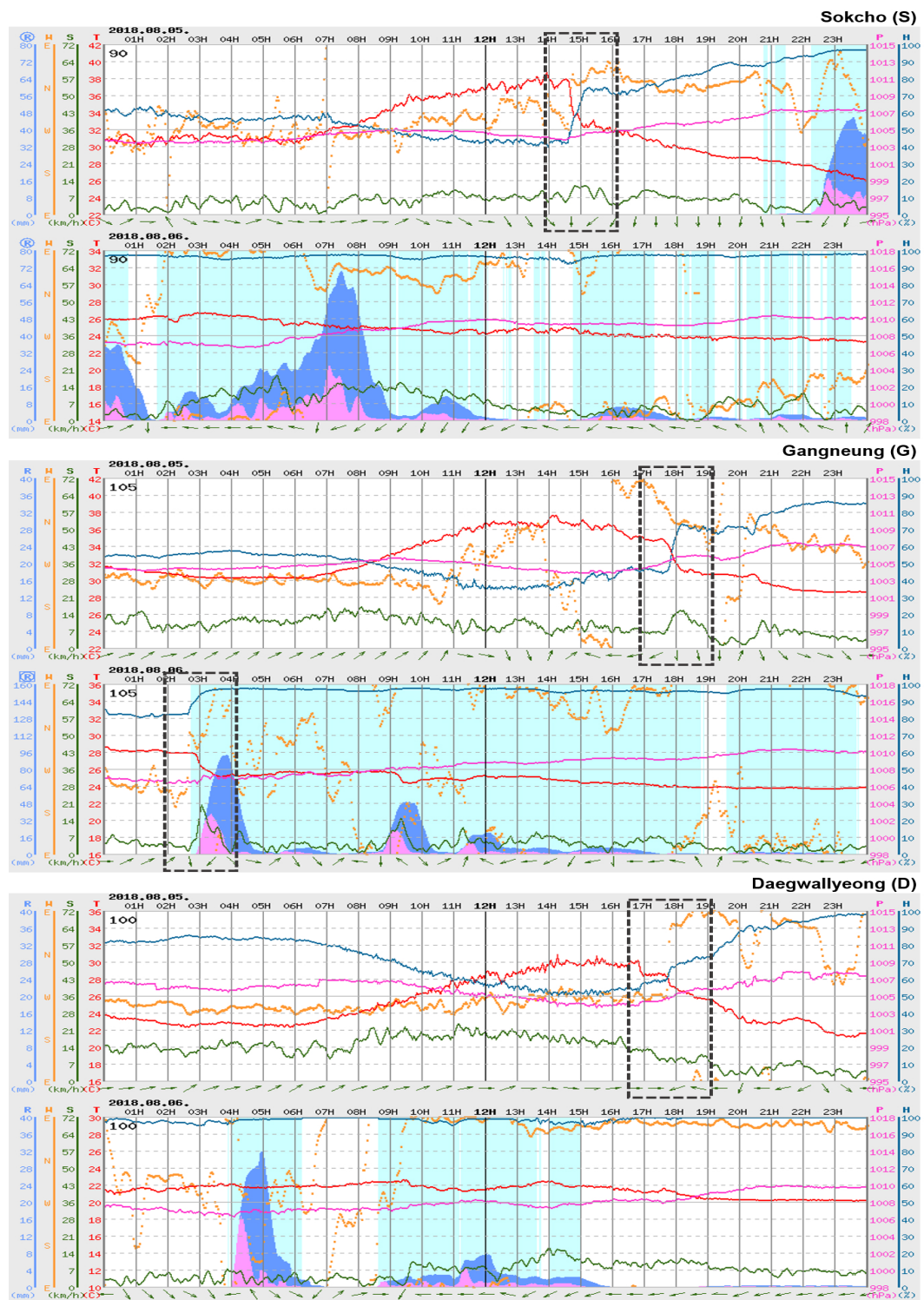


Figure 5. Time series of meteorological variables from Sokcho (top), Gangneung (middle) and Daegwallyeong (bottom) from 00:00 KST 5 to 00:00 KST 7 August 2018 (KST = UTC + 9) for mean sea-level pressure (P; pink), relative humidity (H; dark blue), temperature (T; red), rainfall (R; blue), and 10-min average wind speed (S; dark green) and direction (W; orange). Shaded areas with cyan, pink and blue mean the precipitation period, and the 15-min and 1 h accumulated rainfall amount, respectively. Dashed boxes indicate the period of abrupt changes in H and T. From the KMA ASOS data.

Rainfalls at all stations in Figure 5 were characterized by multi-modal peaks in both 1 h AR (shaded in blue) and 15-min AR (shaded in pink), indicating repeated development of storm cells.

At S, the first rainfall continued for 4 h with the maximum precipitation rate of 35.3 mm/h and total rainfall amount of 83.5 mm. It was produced by the convective cells moved from the coast of North Korea, as shown in Figure 6. The second rainfall recorded the maximum precipitation rate of 54.9 mm/h and total rainfall amount of 192 mm: along with rainfalls afterward, it was associated with the quasi-stationary MCS, under the influence of the Kor'easterlies.

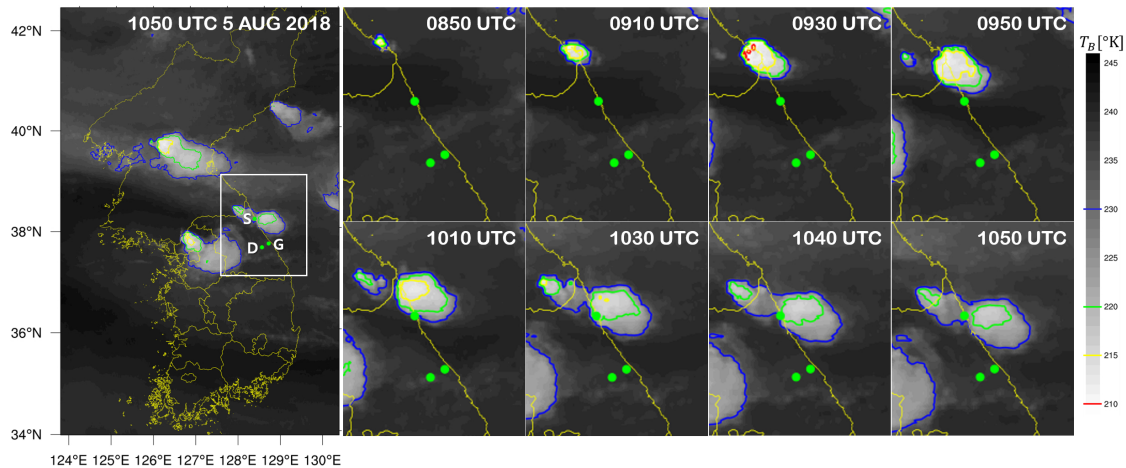


Figure 6. Temporal variation of brightness temperature (T_B , shaded in gray; °K) from the Advanced Himawari Imager (AHI) water vapor band 8. Colored contours indicate $T_B = 210$ °K (red), 215 °K (yellow), 220 °K (green), and 230 °K (blue), respectively. The white rectangle (**left panel**) represents the sub-domain for enlarged images (**right panels**) from 08:50 UTC to 10:50 UTC 5 August 2018. Green dots depict station locations (see Figure 1b).

At G, the first peak of rainfall started as the surface wind changed from southwesterly to north-northwesterly to northeasterly with precipitous increase in speed—a peak of 28.4 km h⁻¹ (not shown). Embedded in the prevailing easterlies, surface winds were quite varying throughout the HRE, especially when the rainfall peaks were related to wind peak speeds: for example, at G, the first, third and fourth rainfall peaks started with wind peak speeds of 28.4 km h⁻¹, 19.4 km h⁻¹ and 13.0 km h⁻¹, respectively (not shown)—evidencing the effect of complex surface flows, especially cold pool outflows.

At D, the first rainfall began as the surface wind changed from northwesterly to easterly. During this precipitation period, winds also blew from the northwest, which might have been related to the mountain breeze and/or outflows from precipitating clouds. During the second rainfall, winds were prevailed by easterlies suggesting that rainfalls occurred by convective clouds formed through the orographic lift of moist air transported by the Kor'easterlies.

4.2.2. Tapering Cloud and Quasi-Stationarity

Figure 7 displays radar reflectivity (Z), superimposed on T_B , for 15:00–22:00 UTC 5 August. Reference [62] showed that the MCS had cloud tops with $T_B \leq -52$ °C (≈ 221 °K), and about 60% of the cold cloud shield area ($T_B \leq 220$ °K) in MCSs had underlying precipitation—both features are well demonstrated in our case. Radar reflectivity is useful to identify the strength and location of convective cells: it is also an effectual measure to characterize precipitation type via a threshold of $Z = 35$ dBZ—stratiform precipitation for $Z < 35$ dBZ and convective precipitation otherwise [62].

The MCS started with a convective cell, which initiated at and moved from North Korea (see Figure 6) and produced the first-peak rainfall at Sokcho (see Figure 5; top panel), then was followed by sequential development of convective cells. At 15:00 UTC, a new deep convective system was instituted over the ES near the border between North Korea and South Korea. As denoted by the cold cloud shield area, the MCS continuously grew during the heavy rainfall period.

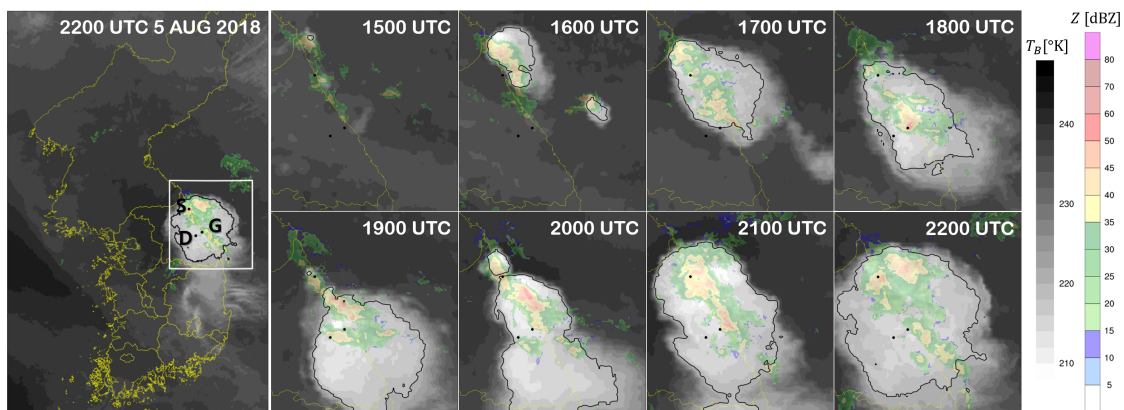


Figure 7. Temporal variation of brightness temperature (T_B , shaded in gray; °K) from the AHI water vapor band 8 and composite radar reflectivities (Z , shaded; dBZ). Black solid lines indicate $T_B = 220$ °K. In terms of reflectivity, total precipitation is divided into stratiform ($Z < 35$ dBZ; shaded in blue to green) and convective ($Z \geq 35$ dBZ; shaded in yellow to pink) components. The white rectangle (left panel) represents the subdomain for enlarged images (right panels) from 15:00 to 22:00 UTC on 5 August 2018. Black dots depict station locations (see Figure 1b).

On 15:00 UTC, convective precipitations ($Z \geq 35$ dBZ) were sporadic over the coast around S, evolved into an MCS on 16:00 UTC, then spread out and moved south-southeastward along the coastline, showing the maximum reflectivity at G on 18:00 UTC. It is notable that on 19:00 UTC new convective cells formed over S at the upwind tip of the tapering cloud while the convective cell, located at G one hour ago, moved to the mountain side (i.e., near D)—possibly through orographic lifting induced by the Kor’easterlies and the cold pool outflows. By 20:00 UTC, the convective cell over S developed into an MCS, whereas the convective reflectivity band at the upwind tip moved southeastward. On 21:00 UTC, the new MCS merged into the main MCS making the upwind cloud boundary arched while the convective band relocated to the east of G. On 22:00 UTC, the MCS enlarged to a circular form with the major convective reflectivities split into two cells: one over S and the other over the adjacent sea. These features evidence the back-building/quasi-stationary development of the MCS.

Lightnings were continuously observed during the HRE, as depicted in Figure 8. Colored crosses represent locations of lightning flashes occurred at previous observation times up to -3 h. For example, blue crosses on 20:00 UTC mean the lightning flashes observed between 18:30 UTC (-1.5 h) and 19:00 UTC (-1 h). Lightnings started on 16:00 UTC 5 August as fresh flashes (observed within 30 min; red crosses) off the coast in the north of Sokcho. Then the fresh lightning flashes repeatedly appeared over the area between Sokcho and Gangneung until 01:00 UTC 6, exhibiting the repeated (i.e., back-building) development of new convective cells therein. Afterwards, the fresh flashes moved southward following the major storm cells.

Figure 9 shows hourly variation of the 12 h ARs. For example, the map on 22:00 UTC 5 August means the 12 h AR for 10:00–22:00 UTC 5, and that on 23:00 UTC 5 denotes the 12 h AR for 11:00–23:00 UTC 5, and so on. Among the stations specified on the maps, Hyeonnae (H) and Seorak-dong (SA) are close to Sokcho (S) while Okgye (O) is close to Gangneung (G). Numbers indicated on the maps represent the area maximum values, with the station acronyms in parentheses. The rainfall started mainly at S on 15:00 UTC 5, then the precipitation system showed multi-cell (dual or triple cells) development along the coastline. From 17:00 to 21:00 UTC 5, the AR peaks appeared at H while rainfall at G also increased; then moving to S (including SA) up to 02:00 UTC 6 with steady increase of rainfall in G. Afterwards, the AR peaks moved southward to G and O until the precipitation system got weakened at 14:00 UTC 6. Meanwhile a new storm cell development is also detected at the north of G (i.e., SA nearby S) on 07:00 UTC 6, indicating the back-building development of convective cells. Overall, the continuous development of convective cells mainly occurred at the north around S until 02:00 UTC 6, then moved to the south nearby G while being weakened. The multi-cell structure also

suggests that dynamical interactions among the convective cells were viable at the boundaries through the storm outflows.

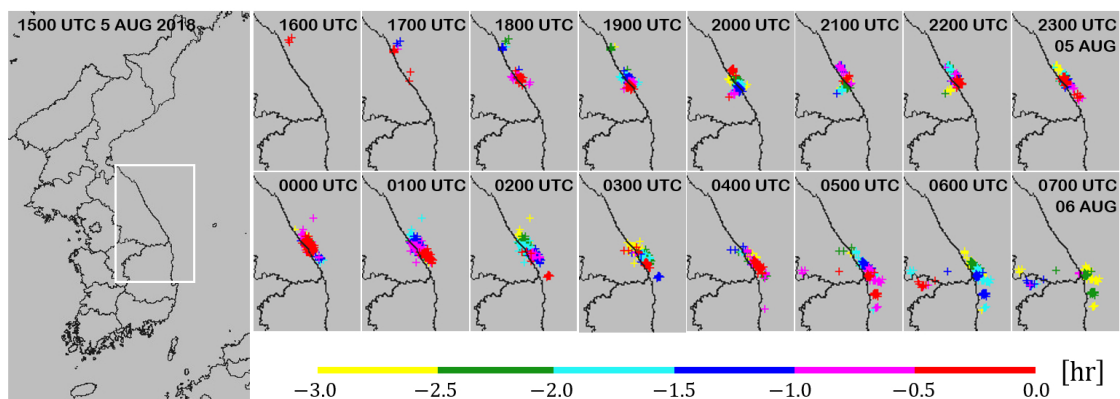


Figure 8. Hourly variation of lightnings from 15:00 UTC 5 to 07:00 UTC 6 August 2018. Each panel represents lightnings occurred during the last 3 h, as indicated in different color per half an hour. The white rectangle (left panel) represents the sub-domain for enlarged images (right panels). From the KMA.

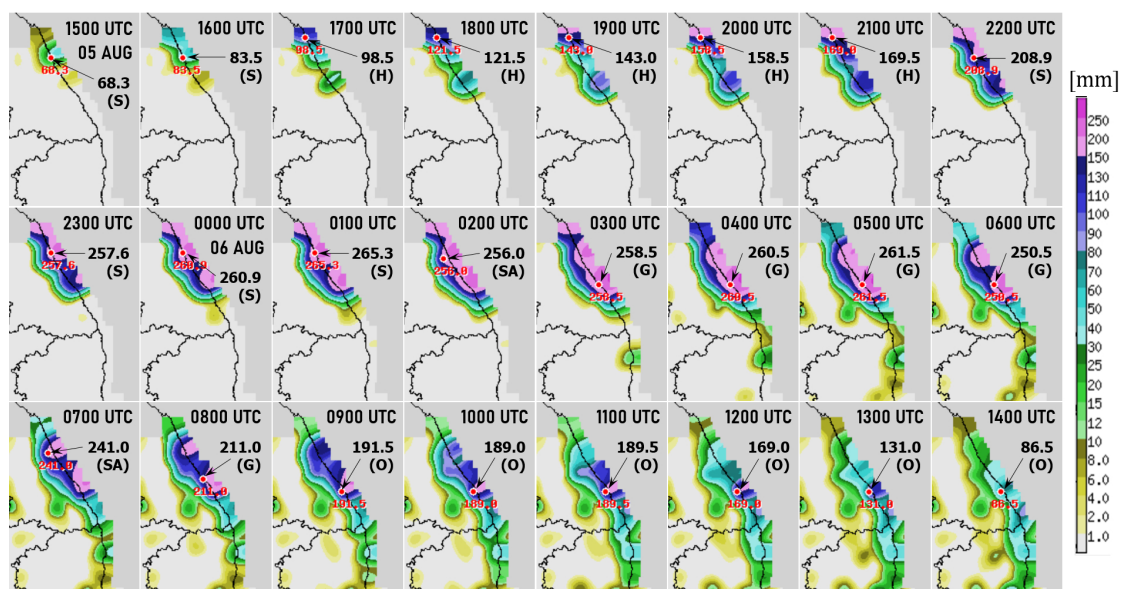


Figure 9. Hourly variation, from 15:00 UTC 5 to 14:00 UTC 6 August 2018, of the 12 h accumulated rainfall (AR; mm) ending at the specified time in each panel over the same enlarged domain in Figure 8 (white rectangle). Numbers indicate the maximum 12 h AR with the stations in parentheses: S for Sokcho, H for Hyeonae (~36 km north-northwest from S), SA for Seorak-dong (~20 km west-southwest from S), G for Gangneung, and O for Okgye (~20 km south-southeast from G). From the KMA.

4.3. Processes in the Modeled Convective System

4.3.1. Moisture Transport and Instability Indices

Figure 10 displays wet-bulb potential temperature (θ_w) and horizontal convergence at 950 hPa, and CAPE, calculated from WRF. On 12:00 UTC 5 August, northeasterlies prevailed over the northern ES while northwesterlies spread over the southern ES, due to L_{TC} near Tohoku (see Figure 3). A moisture band with high θ_w from the ES was carried to the region of repeated convection in Korea by the Kor'easterlies that also caused strong speed convergence at the offshore/coastal zone near Sokcho. Along the moisture band, CAPE was in excess of 1800 J kg^{-1} . On 18:00 UTC, the Kor'easterlies

strengthened over the ES due to expansion of H_{NC} (see Section 4.1). The enhanced Kor'easterlies pushed both the moisture and CAPE bands southwestward—closer to Yeongdong. It is obvious that both Sokcho and Gangneung had higher moisture and CAPE by these movements, implying higher potential for severe thunderstorm development off the coast of Yeongdong. Besides, additional moisture and CAPE were transported from the western part of Korea through northwesterlies, possibly to higher levels (e.g., 925–850 hPa) due to mountains.

Instability indices in Sokcho and Gangneung maintained high values during the nighttime of 5 August: 1130–1410 $J\ kg^{-1}$ for CAPE, above 40 °C for KI, and 260–280 for SWEAT—all indicating great potentials of strong convection and severe thunderstorms. In Korea, MCS and heavy rainfall typically develop with CAPE larger than 1300 $J\ kg^{-1}$ [63].

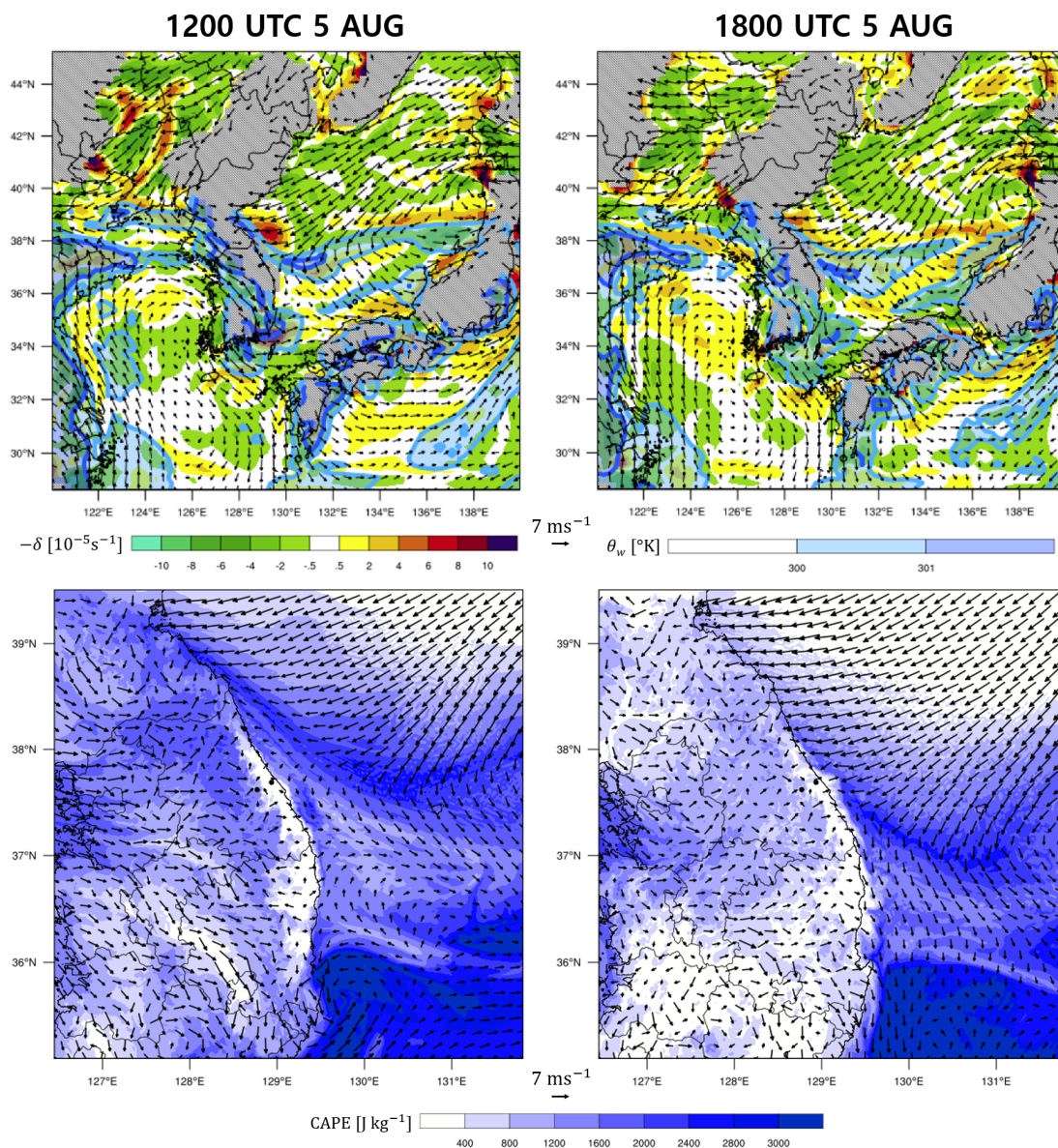


Figure 10. Analyses of storm environment on 12:00 UTC (left panels) and 18:00 UTC 5 (right panels) August 2018. (Upper panels) wet-bulb potential temperature (θ_w , contoured and shaded in blue; °K), horizontal convergence ($-\delta$, shaded; $10^{-5} s^{-1}$) and horizontal wind vectors ($m s^{-1}$) at 950 hPa, over the domain d02 (terrain higher than the 950-hPa level is hatched); (Lower panels) the convective available potential energy (CAPE, shaded in blue; $J\ kg^{-1}$) and surface wind vectors ($m s^{-1}$) over the domain d03.

4.3.2. Domain-Averaged Characteristics of Storm Environment

Figure 11 illustrates temporal and vertical variations of the storm environment, averaged over A1 and A2 (see Figure 1b). Both areas showed similar features except for stronger convection in A2. In the layer 700–400 hPa, water vapor (q_v) stayed almost constant in the early (pre-storm) stage, whereas equivalent potential temperature (θ_e) steadily decreased (Figure 11a,b). Then, both q_v and θ_e increased precipitously, due to strong convection (Figure 11c,d), sustained high values for 8–9 h, then decreased abruptly. The low-level atmosphere, during the pre-storm stage, is characterized by steady increase in θ_e (i.e., getting warmer and moister). Combined with the mid-level cold and dry air, the pre-storm atmospheric environment was characterized by strong potential instability (Figure 11a,b) as well as strong gradients in both q_v and θ_e , especially in 850–700 hPa. At this stage, the surface layer was also characterized by strong potential instability, which diminished later as the whole atmospheric layer showed similarly high θ_e and the maximum q_v : this indicates release of potential instability due to strong updraft (cf. Figure 11c,d).

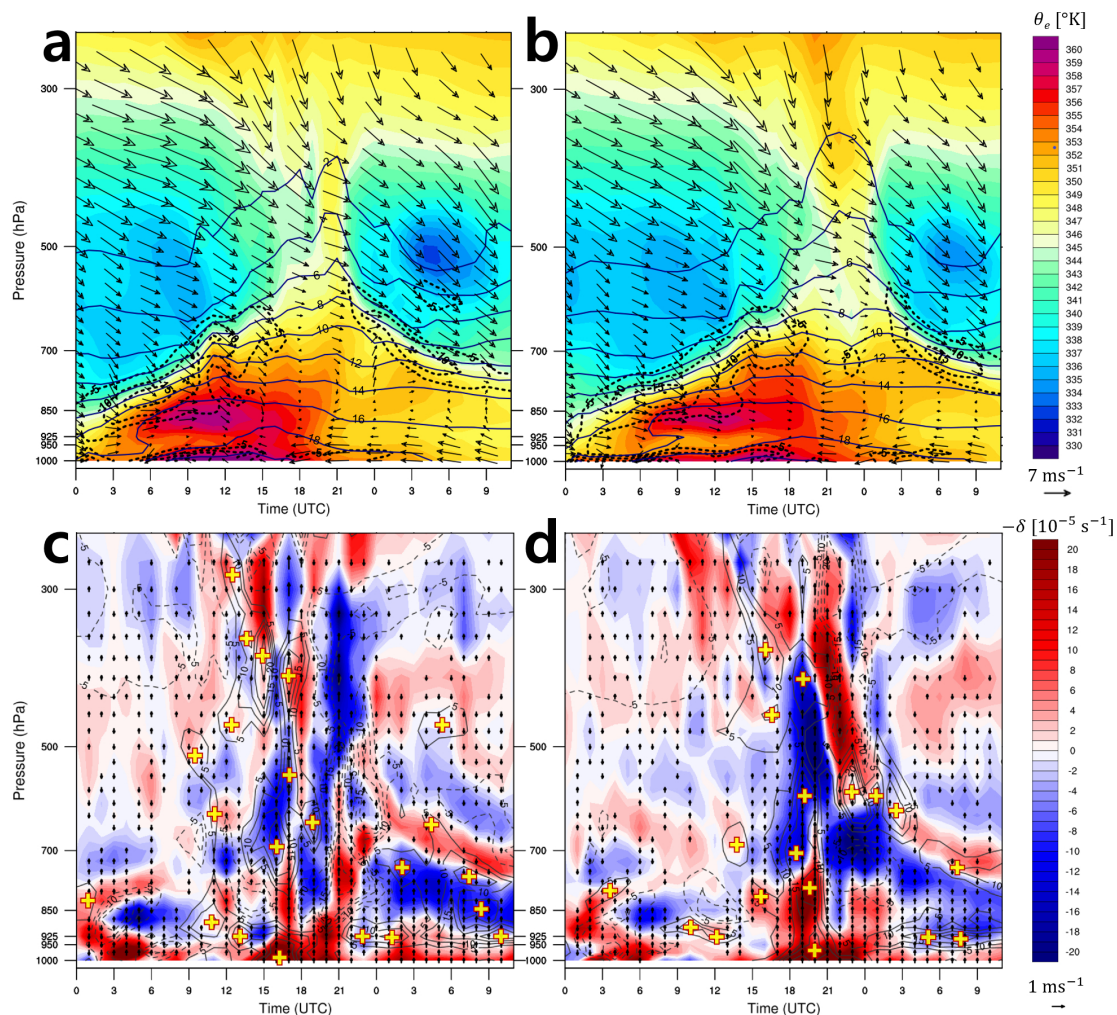


Figure 11. Time–pressure diagrams, averaged over A1 (a,c) and A2 (b,d) (see Figure 1b) from 00:00 UTC 5 to 11:00 UTC 6 August 2018: (a,b) equivalent potential temperature (θ_e , shaded; $^{\circ}\text{K}$), water vapor mixing ratio (q_v , contoured every 2 g kg^{-1}), potential instability (thick dash-contoured every $-5 \text{ }^{\circ}\text{K km}^{-1}$), and horizontal wind vectors (m s^{-1}); and (c, d) horizontal convergence ($-\delta$, shaded; 10^{-5} s^{-1}), vertical component of relative vorticity (contoured every $5 \times 10^{-5} \text{ s}^{-1}$; solid for positive and dashed for negative values) with yellow crosses representing centers of positive values, and vertical wind vectors (m s^{-1}). Values of all the fields are computed over the domain d03.

Surface winds changed from westerlies to easterlies around 06:00 UTC 5, getting stronger and reaching higher with time. Mid-level winds were mostly northwesterlies while upper-level winds turned from northwesterlies to north-northwesterlies, especially during the period of strong convection; thus making the anvil clouds disperse toward south-southeastward along the coastline (see Figure 7). It represented substantial vertical wind shear, in terms of both speed and direction (veering), which is essential for the MCS strength and longevity by enhancing lifting and generating new convective cells through interaction with the cold pool (e.g., [64,65]).

Weak updrafts developed in the early stage due to convergence at the surface layer and divergence at 925–850 hPa (Figure 11c,d); however, no significant updraft developed during the build-up of strong potential instability. Deep convective motion started when the low-level convergence and the mid-to-upper-level divergence strengthened prominently: these vertical motions contributed to release the potential instability (cf. Figure 11a,b), which induced further vigorous convection.

We also note that positive (cyclonic) relative vorticity fields appeared at mid-levels, around 10:00 UTC 5 at 500 and 600 hPa in A1 and on 14:00 UTC at 700 hPa in A2 (see the yellow crosses in Figure 11c,d); then showed the maximum values during the periods of strong low-level convergence and updraft. The time lag between A1 and A2 implies that the mid-level vortices in 700–400 hPa had moved from the north (A1) to the south (A2) along the coastline. Positive vortices also enhanced at the surface layer reaching the maxima at the times of strong updraft—forming updraft-vorticity zones [66] with upright connection to the mid-level vortices, and further enhancing the vertical convection.

Spotting dry intrusion at upper level is crucial in diagnosing deep convection because convective instability is present at the leading part of the dry band due to buoyancy force of cold/dry air over warm/moist air [67]. We can obtain information about atmospheric moisture at different levels via the AHI three water vapor bands [51], whose weighting functions show peak responses near 350–400 hPa for band 8, near 600–700 hPa for band 10, and in-between for band 9—centered at 6.2 μm , 7.3 μm , and 6.9 μm , respectively. Figure 12 represents the three-band water vapor images from AHI on 0900 UTC and 1200 UTC 5 August. A small convective cell near the southeastern coast of North Korea on 0900 UTC evolved into two larger convective cells in the next three hours (see the blue arrows). On 0900 UTC, a prominent dry intrusion is observed in mid-level (the 6.9 μm channel) just the south of the small convective cell (see the red dashed circle), and extends to upper level (see the 6.2 μm channel). In low-level (the 7.3 μm channel), the same area is shaded in light-gray, implying moist air therein. These water vapor images clearly illustrate that low-level moist air is capped by a deep dry layer aloft, which supports our findings in Figure 11. The strong gradient in vertical moisture makes the atmosphere convectively unstable, and induces rapid growth of deep convective cells when combined with proper lifting forcings, as demonstrated by the convective cells on 1200 UTC and the MCS in subsequent hours (see Figure 7). Although the vertical difference of dry/wet conditions is not clearly shown in the same area on 1200 UTC, due to the convective clouds, we have analyzed the relative humidity and temperature fields at 400 hPa and 925 hPa, and noticed cold/dry air aloft and warm/moist air below (not shown).

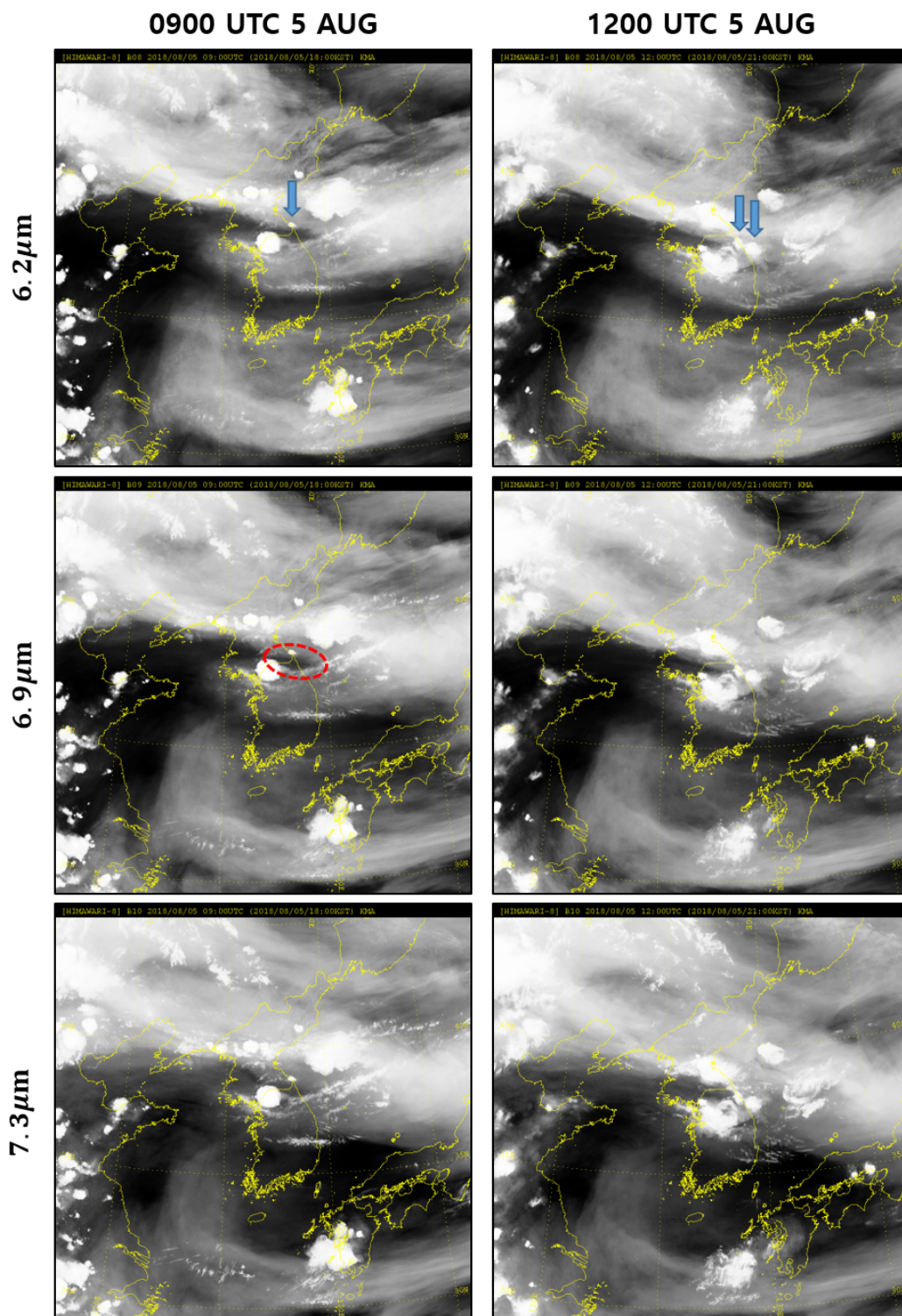


Figure 12. Water vapor images from the AHI three water vapor channels—6.2 μm (top panels), 6.9 μm (middle panels), and 7.3 μm (bottom panels) on 0900 UTC (left panels) and 1200 UTC (right panels) on 5 August 2018. Blue arrows indicate convective cells described in the text, and the red dashed circle depicts the mid-level dry intrusion. From the KMA/National Meteorological Satellite Center.

4.3.3. Triggering and Back-Building Processes

We investigated the processes for initiation and recurrence of convection. We first checked the contribution of the prolonged heat wave over Yeongdong on convection through R_i (see Section 2.3). At 12:00 UTC 5 August, R_i in Yeongdong ranged from 0.25 to 16 at the lowest level, indicating mechanical and thermodynamically-driven lifting jointly contributed to initiation and maintenance of convection in this region (see [59]).

In Figure 13, we examined the impact of cold pool outflow on repeated convection. On 15:00 UTC 5 (Figure 13a), coastal areas of low θ represent cold pools formed from previous rainfalls (see the radar image at 15:00 UTC in Figure 7). At the boundary of the cold pool outflows and the Kor'easterlies, a coastal front was formed—producing updraft (purple area), in which convective cells can easily arise due to transport of moist and conditionally-unstable air over the ES by the Kor'easterlies and the frontal uplifting. By 18:00 UTC (Figure 13b), convective cells developed vigorously at the frontal zone producing heavy rainfall along the front: the northern edge of front moved into the mountain foot due to strong Kor'easterlies, resulting in rainfall at the coastal plain. Some of the cold pool outflows, generated by new convective cells, directed toward the coast and contributed to the orographic rainfall at the mountain foothill. By 20:00 UTC (Figure 13c), the front moved further into the mountain foot, and the cold pools further enhanced as well, making the flows near the coast more complex and producing more rainfall over wider areas. Around S, updraft zones formed at both the mountain foothill and off the coast at the outflow boundaries. The rainfall shape matched very well with the observed tapering cloud and radar echo (cf. Figure 7 on 20:00 UTC). By 22:00 UTC (Figure 13d), the cold pool strengthened and the outflow boundary further intruded toward the mountains between S and G. The rainfall over the mountain crest, at the west of S, occurred through the orographic uplift induced by the strong easterly winds owing to both the outflows and the Kor'easterlies: at the south of S, outflows at the western boundary slowly moved over the mountain producing orographic rainfalls there, whereas outflows at the eastern boundary encountered with the Kor'easterlies, forming an updraft zone along the coastline.

Figure 14 shows vertical cross sections of the MCS along A–B in Figure 13. On 16:00 UTC 5, below 1 km, strong Kor'easterlies abided over the ES at the east of 128.8°E while westerlies blew out from the coast where precipitation occurred. Convective clouds formed at 3–7 km while a new cloud formed at the coast-side of the main rainfall system where the two flows met and made convection. With a closer look below 2 km (bottom left), we notice that lifting of the westerlies also occurred at the boundary of a cold pool formed underneath the main rainfall system. Updrafts were sustained even inside the precipitating area.

On 20:00 UTC 5, the MCS showed maximum growth along A–B, with strong updrafts reaching over 12 km and diverging out at 13–14 km. Rainfalls occurred all over the mountainous coastal areas, including off the coast, with the most intense rainfall at the coast. Besides the orographic lifting and precipitation, the two updraft zones—one at the mountain base and the other off the coast, as described in Figure 13—merged vertically over 6 km making deep convective cloud reaching over 12 km. On 22:00 UTC, typical orographic lifting and its associated deep convective clouds and rainfalls are observed. We also note a new cloud developed over the coastline due to the uplift of inflowing Kor'easterlies at the eastern tip of a cold pool formed beneath the precipitation at the foothill-coast area as well as the speed convergence.

By 00:00 UTC 6, the convective system weakened along A–B as the main system moved southward. Coastal precipitation decreased while non-precipitating orographic clouds still remained on the mountain slope and top. As shown below 2 km (bottom right), the Kor'easterlies made the first updraft at the eastern tip of the coastal cold pool, then the second one at the mountain slope.

Overall, the MCS developed through back-building convection induced by thermodynamically-driven as well as mechanical lifting forcing, associated with the prolonged heat wave, the orographic effect and the low-level convergence, through interactions among the pre-existing cold pool outflows, terrain-induced local flows, and the Kor'easterlies. These factors contributed to continuous

development of deep moist convective cells, under environmental conditions favorable for convection—moist air with high CAPE and low LCL and LFC (Figure 4) and high potential instability (Figure 11). Storm-generated cold pool outflows played a significant role in maintaining the back-building process (e.g., [68]). Localized enhancement of convergence and vertical wind shear along pre-existing (outflow) boundaries also lead to the occurrence of severe local storms (e.g., [69]).

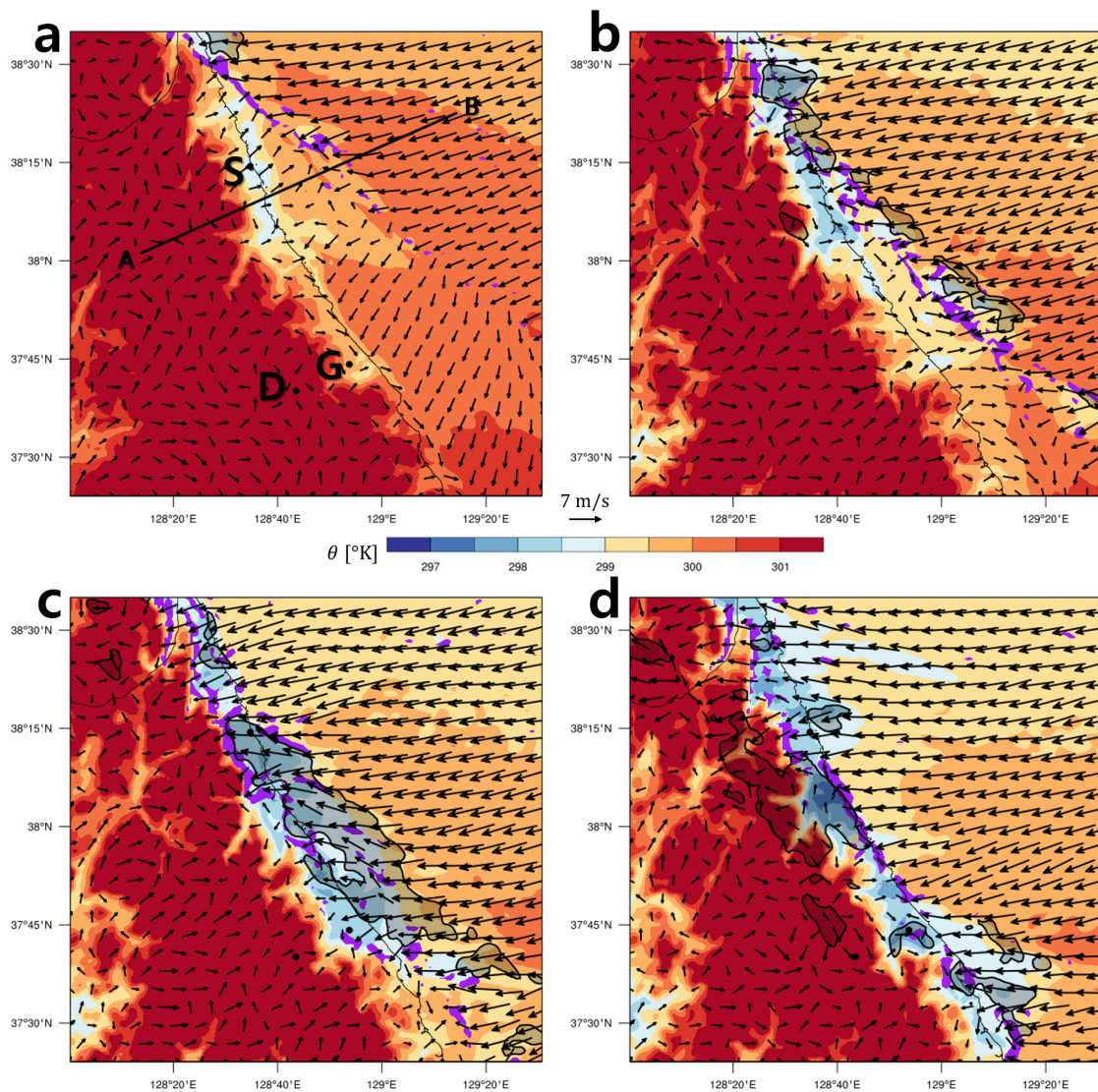


Figure 13. Potential temperature (θ , shaded; $^{\circ}\text{K}$) at the lowest model level, hourly accumulated rainfall greater than 20 mm (hatched with closed contour), vertical wind speed at 500 m greater than 0.5 m s^{-1} (shaded in purple), and horizontal wind vectors at 10 m (m s^{-1}) on (a) 15:00 UTC, (b) 18:00 UTC, (c) 20:00 UTC, and (d) 22:00 UTC 5 August 2018, over the domain d03.

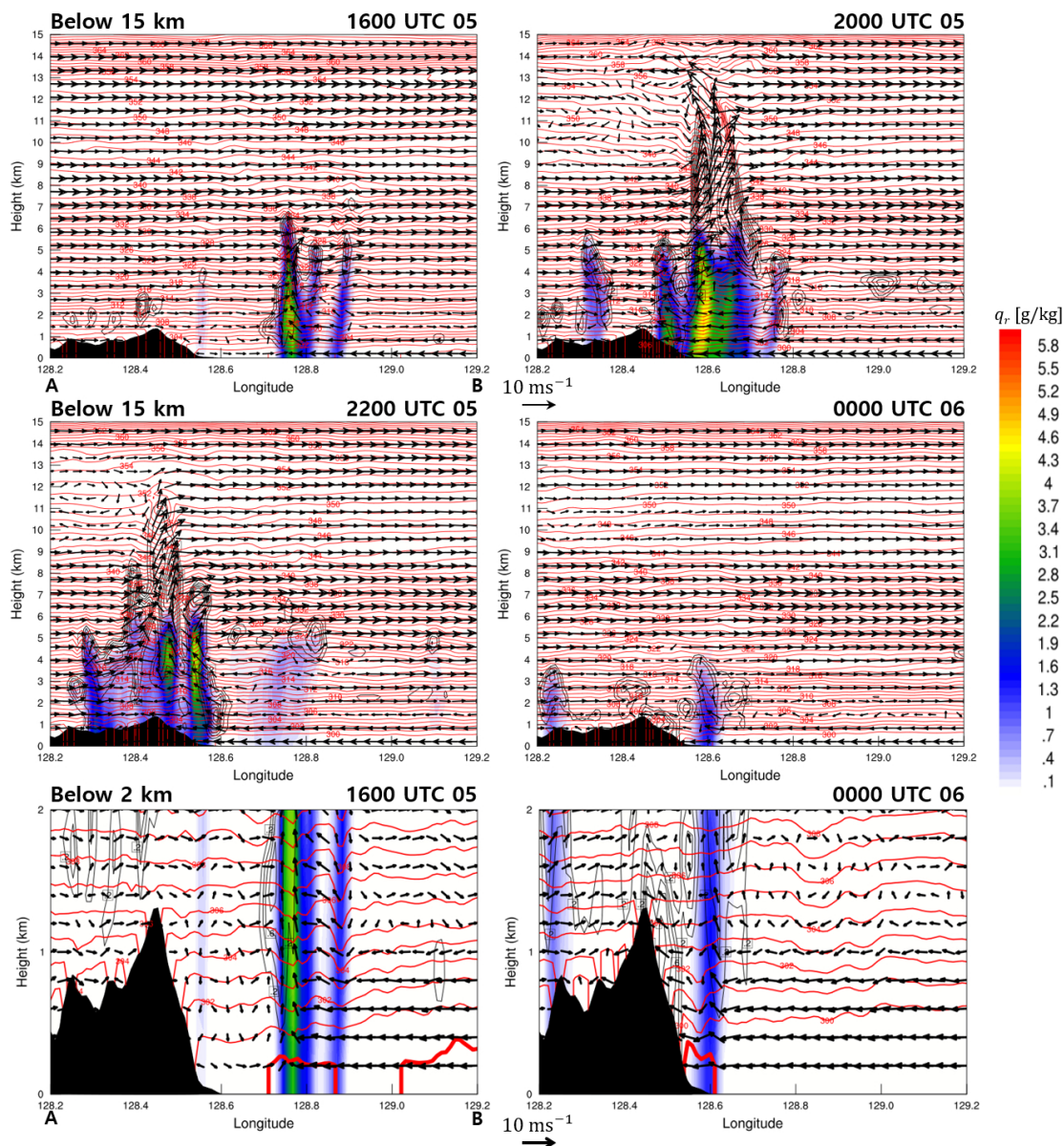


Figure 14. Vertical cross sections of mixing ratios of rain water (q_r , shaded; g kg^{-1}) and cloud water (q_c , contoured every 0.2 g kg^{-1}), potential temperature (θ , red-contoured every $1 \text{ }^\circ\text{K}$), and wind vectors along the axis A–B in Figure 13 below 15 km (top and middle panels) and 2 km (bottom panels) at given specific times. Thin red lines (bottom panels) depict $\theta = 300 \text{ }^\circ\text{K}$ for 16:00 UTC 5 and $\theta = 299 \text{ }^\circ\text{K}$ for 00:00 UTC 6, respectively. Computations are made at the domain d03.

4.3.4. Decaying Process

The MCS decayed due to the weakening of back-building processes, associated with cold pool outflows, low-level moisture supply, potential instability, strong updraft, etc. In Figure 15, changes of such factors in the decaying stage of the MCS are described for 03:00 UTC 6 August. The low-level moisture band from the ES retreated to the south, resulting in cease of moisture supply to the region of back-building convection (Figure 15a) and hence lowering the potential instability (cf. Figure 11a,b). Moreover, heavy rainfall and its associated coastal cold pools as well as the offshore low-level convergence had declined (Figure 15a,b); thus begetting ineffectual convection and less generation of convective cells. As the MCS began to dissipate, Sokcho had weak stratiform rainfall ($Z < 35 \text{ dBZ}$), whereas Gangneung had convective rainfall but much weakened than before (Figure 15c). Since the

MCS propagated south-southeastward along the coastline due to the upper-level north-northwesterlies (see Figures 8 and 9), the convective rainfall at Gangneung terminated after a few hours.

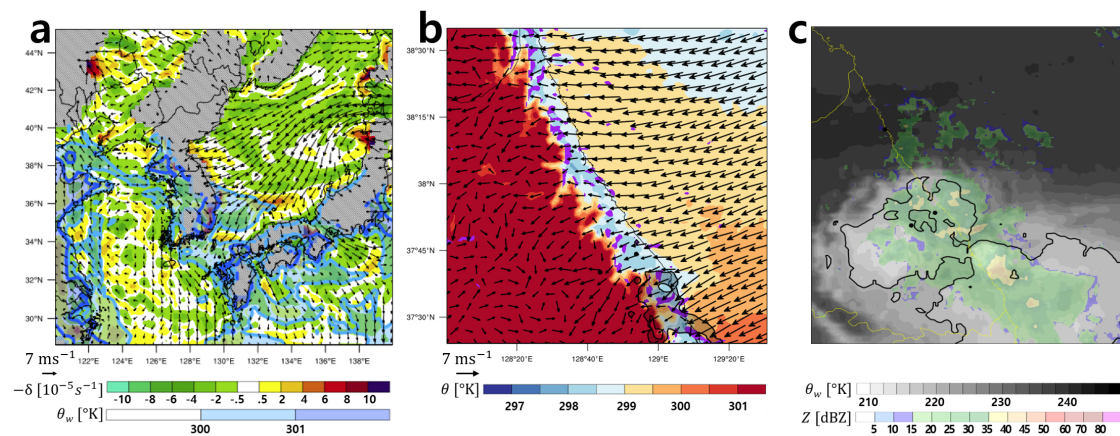


Figure 15. Same as in (a) Figure 10, (b) Figure 13, and (c) Figure 7, respectively, but for 03:00 UTC 6 August 2018.

5. Conclusions

In this study, we investigated a heavy rainfall event (HRE) that caused flash flooding at the mountainous coast in the northeastern part of South Korea, called Yeongdong, which was produced by a quasi-geostationary/back-building mesoscale convective system (MCS) with tapering cloud rarely observed in this region. We performed multi-data analyses of storm environment using the AWS/ASOS observations, the satellite/radar data, and the high-resolution WRF simulations. In particular, the brightness temperature, obtained from the water vapor band 8 of the Advanced Himawari Imager onboard Himawari 8, was useful to identify the existence of MCS and its effective area, whereas the composite radar reflectivity was effectual to divide the total precipitation into the convective and stratiform components by defining a convective reflectivity threshold.

Figure 16 represents essential features of the MCS. Prior to the MCS and tapering cloud development, convective storms, originated from the coastal region of North Korea, produced sporadic rainfalls and cold pools in Yeongdong, whereas the synoptic environment enhanced the Kor'easterlies—winds blowing from the East Sea/Sea of Japan (ES) to the eastern coast of South Korea. The low-level westerlies from the inland Korea as well as the Kor'easterlies conveyed warm and moist air while the mid-to-upper-level northwesterlies carried cold and dry air into this region; thus, building up strong potential instability. The mid-level cyclonic vortices also propagated along the Yeongdong coastal areas.

As the Kor'easterlies approached the coast, a low-level coastal convergence zone formed. A narrow convection band developed along the coastal front offshore Sokcho at the boundary between the cold pool outflows and the Kor'easterlies: the northern edge of the front/convection was located north of Sokcho, triggering the back-building process for the MCS. The potential instability release further enhanced the convection. As both the cold pool outflows and the Kor'easterlies strengthened, the front moved inland and emplaced on the mountain base near Sokcho, effectuating orographic lifting and rainfalls at the foothills: thus, the back-building process continued near Sokcho. A similar process took place near Gangneung with a time lag. The MCS and its associated tapering cloud slowly moved south-southeastward along the coastline due to the upper-level north-northwesterly winds, with the upwind tip stationed near Sokcho. The vertical convection was further enhanced by the mid-level advection of positive relative vorticity ($\zeta > 0$).

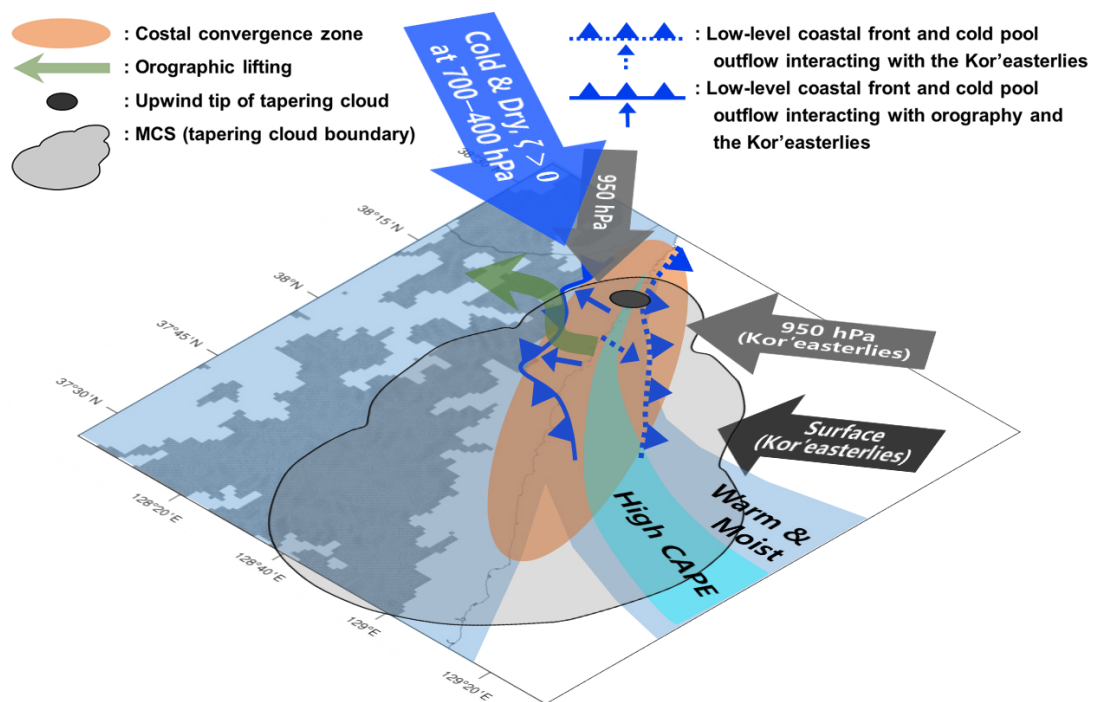


Figure 16. Schematic diagram of the quasi-stationary MCS representing the triggering and back-building processes for the coastal flooding event at the Yeongdong region in South Korea.

This kind of flood-producing MCS with tapering cloud and back-building process, has rarely occurred and been seldom studied in Korea. To improve forecasts of such convective systems in the complex coastal terrain regions, further studies are essentially required on interactions among the prevailing winds, cold pools, orography, and local circulation systems, and their combined effect on the back-building process.

Although this study is focused on a coastal MCS in Korea, the findings here can provide basic knowledge on similar coastal convections in other parts of the world, especially under extremely warm atmospheric environment and with complex coastal terrains. In a warming climate, consecutive occurrence of contrasting extreme events, like this case, may become more common; thus, understanding the development mechanism of extreme precipitation under the extreme heat wave condition is of utmost importance. Further study is required to investigate possible linkage between global warming and the flood-producing heavy rainfall event under the extremely warm condition, especially in the context of super Clausius–Clapeyron relationship.

Author Contributions: S.K.P. contributed to conceptualization; experiment and validation design; writing of submitted and revised manuscript, review and editing, and responses to reviewers; formal analyses; supervision; funding acquisition; and project administration. S.P. contributed to performing experiments and validations; writing first draft; data acquisition and handling; software; and graphical analyses. All authors have read and agreed to the published version of the manuscript.

Funding: This work was funded by the Korea Meteorological Administration Research and Development Program under Grant KMIPA (KMI2018-06710), and partly supported by Basic Science Research Program through the National Research Foundation of Korea(NRF) funded by the Ministry of Education(2018R1A6A1A08025520).

Acknowledgments: The NCEP FNL Operational Model Global Tropospheric Analyses data are available from the Research Data Archive: <https://rda.ucar.edu/datasets/ds083.2/>. The composite radar reactivity/radar-AWS rain-rate (RAR) data, ASOS/AWS data, and Himawari-8 data are available from the Korea Meteorological Administration (KMA) database: <http://203.247.66.28/> (instructed in Korean), in which a user registration is required. Weather charts at standard pressure levels and auxiliary charts can also be obtained through KMA at <http://www.weather.go.kr/>. The KMA/National Meteorological Satellite Center has kindly provided us with the AHI water vapor images.

Conflicts of Interest: The authors declare no conflict of interest.

References

1. Park, S.K.; Lee, E. Synoptic features of orographically enhanced heavy rainfall on the east coast of Korea associated with Typhoon Rusa (2002). *Geophys. Res. Lett.* **2007**, *34*, L02803. [[CrossRef](#)]
2. Jung, S.H.; Im, E.S.; Han, S.O. The effect of topography and sea surface temperature on heavy snowfall in the Yeongdong region: A case study with high resolution WRF simulation. *Asia-Pac. J. Atmos. Sci.* **2012**, *48*, 259–273. [[CrossRef](#)]
3. Lee, J.-G.; Xue, M. A study on a snowband associated with a coastal front and cold-air damming event of 3–4 February 1998 along the eastern coast of the Korean Peninsula. *Adv. Atmos. Sci.* **2013**, *30*, 263–279. [[CrossRef](#)]
4. Nam, H.G.; Kim, B.-G.; Han, S.-O.; Lee, C.; Lee, S.-S. Characteristic of easterly-induced snowfall in Yeongdong and its relationship to air-sea temperature difference. *Asia-Pac. J. Atmos. Sci.* **2014**, *50*, 541–552. [[CrossRef](#)]
5. Park, S.K. Terminological review and suggestion on the easterlies in Yeongdong and Donghae-Seonpoong. In *Preprints of the Korea Meteorological Society 2018 Autumn Meeting*; Korea Meteorological Society: Seoul, Korea, 2018; p. 161. (In Korean)
6. Lapenta, W.M.; Seaman, N.L. A numerical investigation of east coast cyclogenesis during the cold-air damming event of 27–28 February 1982. Part II: Importance of physical mechanisms. *Mon. Weather Rev.* **1992**, *120*, 52–76. [[CrossRef](#)]
7. Li, J.; Chen, Y.-L. Barrier jets during TAMEX. *Mon. Weather Rev.* **1998**, *126*, 959–971. [[CrossRef](#)]
8. Revell, M.J.; Copeland, J.H.; Larsen, H.R.; Wratt, D.S. Barrier jets around the Southern Alps of New Zealand and their potential to enhance alpine rainfall. *Atmos. Res.* **2002**, *61*, 277–298. [[CrossRef](#)]
9. Srock, A.F.; Bosart, L.F. Heavy precipitation associated with southern Appalachian cold-air damming and Carolina coastal frontogenesis in advance of weak landfalling Tropical Storm Marco (1990). *Mon. Weather Rev.* **2009**, *137*, 2448–2470. [[CrossRef](#)]
10. Jessup, S.M.; Colucci, S.J. Organization of flash-flood-producing precipitation in the northeast United States. *Weather Forecast.* **2012**, *27*, 345–361. [[CrossRef](#)]
11. Bluestein, H.B. Mesoscale convective systems. In *Severe Convective Storms and Tornadoes: Observations and Dynamics*; Springer: Berlin, Germany, 2013; pp. 265–306.
12. Nishiyama, K.; Iwai, M.; Koyanagi, S.; Fujisaki, N.; Sato, K. Relationships between heavy rainfall disasters and tapering clouds. *J. Jpn. Soc. Civ. Eng. Ser. B1 (Hydraul. Eng.)* **2011**, *67*, I_487–I_492. [[CrossRef](#)]
13. Schumacher, R.S.; Johnson, R.H. Organization and environmental properties of extreme-rain-producing mesoscale convective systems. *Mon. Weather Rev.* **2005**, *133*, 961–976. [[CrossRef](#)]
14. Ducrocq, V.; Nuissier, O.; Ricard, D.; Lebeaupin, C.; Thouvenin, T. A numerical study of three catastrophic precipitating events over southern France. II: Mesoscale triggering and stationarity factors. *Quart. J. Roy. Meteor. Soc.* **2008**, *134*, 131–145. [[CrossRef](#)]
15. Bresson, E.; Ducrocq, V.; Nuissier, O.; Ricard, D.; de Saint-Aubin, C. Idealized numerical simulations of quasi-stationary convective systems over the Northwestern Mediterranean complex terrain. *Quart. J. Roy. Meteor. Soc.* **2012**, *138*, 1751–1763. [[CrossRef](#)]
16. Duffourg, F.; Lee, K.; Ducrocq, V.; Flamant, C.; Chazette, P.; Di Girolamo, P. Role of moisture patterns in the backbuilding formation of HyMeX IOP13 heavy precipitation systems. *Quart. J. Roy. Meteor. Soc.* **2018**, *144*, 291–303. [[CrossRef](#)]
17. Lee, K.-O.; Flamant, C.; Duffourg, F.; Ducrocq, V.; Chaboureaud, J.P. Impact of upstream moisture structure on a back-building convective precipitation system in south-eastern France during HyMeX IOP13. *Atmos. Chem. Phys.* **2018**, *18*, 16845–16862. [[CrossRef](#)]
18. Smith, R.B. The influence of mountains on the atmosphere. *Adv. Geophys.* **1979**, *21*, 87–230.
19. Houze, R.A., Jr. Orographic effects on precipitating clouds. *Rev. Geophys.* **2012**, *50*, RG1001. [[CrossRef](#)]
20. Trier, S.B.; Chen, F.; Manning, K.M. A study of convection initiation in a mesoscale model using high-resolution land surface initial conditions. *Mon. Weather Rev.* **2004**, *132*, 2954–2976. [[CrossRef](#)]
21. Ćurić, M.; Janc, D. Differential heating influence on hailstorm vortex pair evolution. *Quart. J. Roy. Meteor. Soc.* **2012**, *138*, 72–80. [[CrossRef](#)]

22. Shimpo, A.; Takemura, K.; Wakamatsu, S.; Togawa, H.; Mochizuki, Y.; Takekawa, M.; Tanaka, S.; Yamashita, K.; Maeda, S.; Kurora, R.; et al. Primary factors behind the Heavy Rain Event of July 2018 and the subsequent heat wave in Japan. *Sci. Online Lett. Atmos.* **2019**, *15A*, 13–18. [[CrossRef](#)]
23. Wang, S.S.-Y.; Kim, H.; Coumou, D.; Yoon, J.-H.; Zhao, L.; Gillies, R.R. Consecutive extreme flooding and heat wave in Japan: Are they becoming a norm? *Atmos. Sci. Lett.* **2019**, *20*, e933. [[CrossRef](#)]
24. Tsuguti, H.; Seino, N.; Kawase, H.; Imada, Y.; Nakaegawa, T.; Takayabu, I. Meteorological overview and mesoscale characteristics of the Heavy Rain Event of July 2018 in Japan. *Landslides* **2019**, *16*, 363–371. [[CrossRef](#)]
25. Takemi, T.; Unuma, T. Diagnosing environmental properties of the July 2018 Heavy Rainfall Event in Japan. *Sci. Online Lett. Atmos.* **2019**, *15*, 60–65. [[CrossRef](#)]
26. Lenderink, G.; Barbero, R.; Loriaux, J.M.; Fowler, H.J. Super Clausius-Clapeyron scaling of extreme hourly convective precipitation and its relation to large-scale atmospheric conditions. *J. Clim.* **2017**, *30*, 6037–6052. [[CrossRef](#)]
27. Fieuzal, R.; Duchemin, B.; Jarlan, L.; Zribi, M.; Baup, F.; Merlin, O.; Hagolle, O.; Garatuza-Payan, J. Combined use of optical and radar satellite data for the monitoring of irrigation and soil moisture of wheat crops. *Hydrol. Earth Syst. Sci.* **2011**, *15*, 1117–1129. [[CrossRef](#)]
28. Vinukollu, R.K.; Wood, E.F.; Ferguson, C.R.; Fisher, J.B. Global estimates of evapotranspiration for climate studies using multi-sensor remote sensing data: Evaluation of three process-based approaches. *Remote Sens. Environ.* **2011**, *115*, 801–823. [[CrossRef](#)]
29. Sieglaff, J.M.; Hartung, D.C.; Feltz, W.F.; Cronics, L.M.; Lakshmanan, V. A satellite-based convective cloud object tracking and multipurpose data fusion tool with application to developing convection. *J. Atmos. Ocean. Technol.* **2013**, *30*, 510–525. [[CrossRef](#)]
30. El-Askary, H.; Park, S.K.; Ahn, M.H.; Prasad, A.; Kafatos, M. On the detection and monitoring of the transport of an Asian dust storm using multi-sensor satellite remote sensing. *J. Environ. Inform.* **2015**, *25*, 99–116. [[CrossRef](#)]
31. Zhang, X.; Chen, N.; Li, J.; Chen, Z.; Niyogi, D. Multi-sensor integrated framework and index for agricultural drought monitoring. *Remote Sens. Environ.* **2017**, *188*, 141–163. [[CrossRef](#)]
32. Miglietta, M.; Laviola, S.; Malvaldi, A.; Conte, D.; Levizzani, V.; Price, C. Analysis of tropical-like cyclones over the Mediterranean Sea through a combined modeling and satellite approach. *Geophys. Res. Lett.* **2013**, *40*, 2400–2405. [[CrossRef](#)]
33. Wapler, K.; Harnisch, F.; Pardowitz, T.; Senf, F. Characterisation and predictability of a strong and a weak forcing severe convective event—A multi-data approach. *Meteorol. Z.* **2015**, *24*, 393–410. [[CrossRef](#)]
34. Yucel, I.; Onen, A.; Yilmaz, K.K.; Gochis, D.J. Calibration and evaluation of a flood forecasting system: Utility of numerical weather prediction model, data assimilation and satellite-based rainfall. *J. Hydrol.* **2015**, *523*, 49–66. [[CrossRef](#)]
35. Lagasio, M.; Parodi, A.; Pulvirenti, L.; Meroni, A.; Boni, G.; Pierdicca, N.; Marzano, F.; Luini, L.; Venuti, G.; Realini, E.; et al. A synergistic use of a high-resolution numerical weather prediction model and high-resolution Earth observation products to improve precipitation forecast. *Remote Sens.* **2019**, *11*, 2387. [[CrossRef](#)]
36. Kaskaoutis, D.G.; Nastos, P.T.; Kosmopoulos, P.G.; Kambezidis, H.D. The combined use of satellite data, air-mass trajectories and model applications for monitoring dust transport over Athens, Greece. *Int. J. Remote Sens.* **2010**, *31*, 5089–5109. [[CrossRef](#)]
37. Zhang, J.-H.; Yao, F.-M.; Liu, C.; Yang, L.-M.; Boken, V.K. Detection, emission estimation and risk prediction of forest fires in China using satellite sensors and simulation models in the past three decades—An overview. *Int. J. Environ. Res. Public Health* **2011**, *8*, 3156–3178. [[CrossRef](#)] [[PubMed](#)]
38. Morrison, H.; Thompson, G.; Tatarskii, V. Impact of cloud microphysics on the development of trailing stratiform precipitation in a simulated squall line: Comparison of one-and two-moment schemes. *Mon. Weather Rev.* **2009**, *137*, 991–1007. [[CrossRef](#)]
39. Igel, A.L.; Igel, M.R.; van den Heever, S.C. Make it a double? Sobering results from simulations using single-moment microphysics schemes. *J. Atmos. Sci.* **2015**, *72*, 910–925. [[CrossRef](#)]
40. Mlawer, E.J.; Taubman, S.J.; Brown, P.D.; Iacono, M.J.; Clough, S.A. Radiative transfer for inhomogeneous atmospheres: RRTM, a validated correlated-k model for the longwave. *J. Geophys. Res. Atmos.* **1997**, *102*, 16663–16682. [[CrossRef](#)]

41. Dudhia, J. Numerical study of convection observed during the winter monsoon experiment using a mesoscale two-dimensional model. *J. Atmos. Sci.* **1989**, *46*, 3077–3107. [[CrossRef](#)]
42. Oleson, K.W.; Lawrence, D.M.; Bonan, G.B.; Flanner, M.G.; Kluzek, E.; Lawrence, P.J.; Levis, S.; Swenson, S.C.; Thornton, P.E. *Technical Description of Version 4.0 of the Community Land Model (CLM)*; NCAR Technical Note NCAR/TN-478+STR; National Center for Atmospheric Research: Boulder, CO, USA, 2010; p. 257.
43. Lawrence, D.M.; Oleson, K.W.; Flanner, M.G.; Thornton, P.E.; Swenson, S.C.; Lawrence, P.J. Parameterization improvements and functional and structural advances in version 4 of the Community Land Model. *J. Adv. Model. Earth Syst.* **2011**, *3*, 1–27.
44. Hong, S.Y.; Noh, Y.; Dudhia, J. A new vertical diffusion package with an explicit treatment of entrainment processes. *Mon. Weather Rev.* **2006**, *134*, 2318–2341. [[CrossRef](#)]
45. Kain, J.S. The Kain–Fritsch convective parameterization: an update. *J. Appl. Meteor.* **2004**, *43*, 170–181. [[CrossRef](#)]
46. Suk, M.-K.; Chang, K.-H.; Cha, J.-W.; Kim, K.-E. Operational real-time adjustment of radar rainfall estimation over the South Korea region. *J. Meteor. Soc. Jpn.* **2013**, *91*, 545–554. [[CrossRef](#)]
47. Jung, S.-P.; Kwon, T.-Y.; Han, S.-O.; Jeong, J.-H.; Shim, J.; Choi, B.-C. Thermodynamic characteristics associated with localized torrential rainfall events in the southwest region of the Korean Peninsula. *Asia-Pac. J. Atmos. Sci.* **2015**, *51*, 229–237. [[CrossRef](#)]
48. Lee, J.-K.; Kim, J.-H.; Suk, M.-K. Application of bias correction methods to improve the accuracy of quantitative radar rainfall in Korea. *Atmos. Meas. Tech. Discuss.* **2015**, *8*, 4011–4047. [[CrossRef](#)]
49. Park, S.; Park, S.K.; Lee, J.W.; Park, Y. Geostatistical assessment of warm-season precipitation observations in Korea based on the composite precipitation and satellite water vapor data. *Hydrol. Earth Syst. Sci.* **2018**, *22*, 3435–3452. [[CrossRef](#)]
50. Berne, A.; Krajewski, W.F. Radar for hydrology: Unfulfilled promise or unrecognized potential? *Adv. Water Resour.* **2013**, *51*, 357–366. [[CrossRef](#)]
51. Bessho, K.; Date, K.; Hayashi, M.; Ikeda, A.; Imai, T.; Inoue, H.; Kumagai, Y.; Miyakawa, T.; Murata, H.; Ohno, T.; et al. An introduction to Himawari-8/9—Japan’s new-generation geostationary meteorological satellites. *J. Meteor. Soc. Jpn.* **2016**, *94*, 151–183. [[CrossRef](#)]
52. Okuyama, A.; Andou, A.; Date, K.; Hosaka, K.; Mori, N.; Murata, H.; Tabata, T.; Takahashi, M.; Yoshino, R.; Bessho, K. Preliminary validation of Himawari-8/AHI navigation and calibration. In Proceedings of the SPIE 9607, Earth Observing Systems XX, San Diego, CA, USA, 7 July 2015; p. 96072E.
53. Lee, S.; Han, H.; Im, J.; Jang, E.; Lee, M.-I. Detection of deterministic and probabilistic convection initiation using Himawari-8 Advanced Himawari Imager data. *Atmos. Meas. Tech.* **2017**, *10*, 1859–1874. [[CrossRef](#)]
54. Lee, Y.-K.; Li, J.; Li, Z.; Schmit, T. Atmospheric temporal variations in the pre-landfall environment of Typhoon Nangka (2015) observed by the Himawari-8 AHI. *Asia-Pac. J. Atmos. Sci.* **2017**, *53*, 431–443. [[CrossRef](#)]
55. Hirose, H.; Shige, S.; Yamamoto, M.K.; Higuchi, A. High temporal rainfall estimations from Himawari-8 multiband observations using the random-forest machine-learning method. *J. Meteor. Soc. Jpn.* **2019**, *97*, 689–710. [[CrossRef](#)]
56. George, J.J. *Weather Forecasting for Aeronautics*; Academic Press: Cambridge, MA, USA, 1960; p. 673.
57. Miller, R.C. *Notes on Analysis and Severe Storm Forecasting Procedures of The Air Force Global Weather Central*; Tech. Rept. 200(R); Air Weather Service: Offutt Air Force Base, NE, USA; US Air Force: Washington, DC, USA, 1972; p. 184.
58. Jung, S.-P.; In, S.-R.; Kim, H.-n.; Sim, J.; Han, S.-O.; Choi, B.-C. Classification of atmospheric vertical environment associated with heavy rainfall using long-term radiosonde observational data, 1997–2013. *Atmosphere* **2015**, *25*, 611–622. (In Korean with English abstract) [[CrossRef](#)]
59. Sparrow, E.M.; Eichhorn, R.; Gregg, J.L. Combined forced and free convection in a boundary layer flow. *Phys. Fluid* **1959**, *2*, 319–328. [[CrossRef](#)]
60. Doswell, C.A., III. Severe convective storms—An overview. In *Severe Convective Storms*; Meteorological Monographs; Doswell, C.A., III, Ed.; American Meteorological Society: Boston, MA, USA, 2001; Volume 28, pp. 1–26.
61. Chakraborty, S.; Fu, R.; Massie, S.T.; Stephens, G. Relative influence of meteorological conditions and aerosols on the lifetime of mesoscale convective systems. *Proc. Natl. Acad. Sci. USA* **2016**, *113*, 7426–7431. [[CrossRef](#)]

62. Jirak, I.L.; Cotton, W.R.; McAnelly, R.L. Satellite and radar survey of mesoscale convective system development. *Mon. Weather Rev.* **2003**, *131*, 2428–2449. [[CrossRef](#)]
63. Lee, J.-W.; Min, K.-H. Analysis of an outflow boundary induced heavy rainfall that occurred in the Seoul metropolitan area. *Atmosphere* **2017**, *27*, 455–466. (In Korean with English abstract)
64. Rotunno, R.; Klemp, J.B.; Weisman, M.L. A theory for strong, long-lived squall lines. *J. Atmos. Sci.* **1988**, *45*, 463–485. [[CrossRef](#)]
65. Fritsch, J.M.; Forbes, G.S. Mesoscale convective systems. In *Severe Convective Storms*; Meteorological Monographs; Doswell, C.A., III, Ed.; American Meteorological Society: Boston, MA, USA, 2001; Volume 28, pp. 323–357.
66. Brandes, E.A. Finestructure of the Del City-Edmond tornadic mesocirculation. *Mon. Weather Rev.* **1981**, *109*, 635–647. [[CrossRef](#)]
67. Georgiev, C.; Santurette, P.; Maynard, K. *Weather Analysis and Forecasting: Applying Satellite Water Vapor Imagery and Potential Vorticity Analysis*, 2nd ed.; Academic Press: Cambridge, MA, USA, 2016; p. 343.
68. Johnson, R.H.; Mapes, B.E. Mesoscale Processes and Severe Convective Weather. In *Severe Convective Storms*; Meteorological Monographs; Doswell, C.A., III, Ed.; American Meteorological Society: Boston, MA, USA, 2001; Volume 28, pp. 71–122.
69. Maddox, R.A.; Hoxit, L.R.; Chappell, C.F. A study of tornadic thunderstorm interactions with thermal boundaries. *Mon. Weather Rev.* **1980**, *108*, 322–336. [[CrossRef](#)]



© 2020 by the authors. Licensee MDPI, Basel, Switzerland. This article is an open access article distributed under the terms and conditions of the Creative Commons Attribution (CC BY) license (<http://creativecommons.org/licenses/by/4.0/>).